A Unified Vegetation Index for Quantifying the Terrestrial Biosphere

Gustau Camps-Valls,[1*] Manuel Campos-Taberner,[2] Álvaro Moreno-Martínez,[1,9] Sophia Walther,[3] Grégory Duveiller,[4] Alessandro Cescatti,[4] Miguel D. Mahecha,[5] Jordi Muñoz-Marí,[1] Francisco Javier García-Haro,[2] Luis Guanter,[6] Martin Jung,[3] John A. Gamon,[7,8] Markus Reichstein,[3] Steven W. Running[9]

[1]Image Processing Laboratory, Universitat de València, 46980, Paterna, Spain

[2]Earth Sciences Department, Universitat de València, 46100, Burjassot, Spain

[3]Max Planck Institute for Biogeochemistry, 07745 Jena, Germany

[4]European Commission Joint Research Centre, Ispra, Italy

[5]Remote Sensing Centre for Earth System Research, Leipzig University, 04103 Leipzig, Germany

[6]Universitat Politècnica de València, 46022 València, Spain

[7]University of Alberta, Edmonton, Alberta, Canada

[8]University of Nebraska - Lincoln, Lincoln Nebraska, USA

[9]Numerical Terradynamic Simulation Group (NTSG), University of Montana, Missoula, USA

[*]To whom correspondence should be addressed; E-mail: gustau.camps@uv.es

Abstract —

Empirical vegetation indices derived from spectral reflectance data are widely used in remote sensing of the biosphere, as they represent robust proxies for canopy structure, leaf pigment content and, subsequently, plant photosynthetic potential. Here we generalize the broad family of commonly used vegetation indices by exploiting all higher-order relations between the spectral channels involved. This results in a higher sensitivity to vegetation biophysical and physiological parameters. The presented nonlinear generalization of the celebrated Normalized Difference Vegetation Index (NDVI) consistently improves accuracy in monitoring key parameters, such as leaf area index, gross primary productivity, and sun-induced chlorophyll fluorescence. Results suggest that the statistical approach maximally exploits the spectral information, and addresses long-standing problems in satellite Earth Observation of the terrestrial biosphere. The nonlinear NDVI will allow more accurate measures of terrestrial carbon source/sink dynamics and potentials for stabilizing atmospheric CO_2 and mitigating global climate change.

Introduction

Quantifying vegetation cover, biochemistry, structure and functioning from space is key to study and understand global change, biodiversity and agriculture. In practice, remote sensing has relied vastly on the use (and abuse) of vegetation indices (VIs) derived from spectral reflectance due to their generally decent performance. Vegetation indices are parametric transformations of a few spectral bands designed to maximizing their sensitivity to particular biophysical phenomena (e.g. greenness, water content or photosynthetic activity) while minimizing their sensitivity to factors such as soil properties, solar illumination, atmospheric conditions, and sensor viewing geometry. A plethora of narrow-band indices has been proposed in the literature (*1*). Indices are designed for specific applications and conditions, and their parameters are fixed empirically.

The most widely-used vegetation index in Earth observation is undoubtedly the normalized difference vegetation index (NDVI) (*2, 3*). This index exploits the fact that green healthy vegetation shows contrasting behaviour in how it reflects red and near-infrared (NIR) radiation. The more chlorophyll there is in a canopy, the more visible light (including the red) can potentially be absorbed to drive photosynthesis, and thus the higher the absorbed energy that can potentially be consumed in carbon fixation. On the other hand, as more living plant biomass is present, the vegetation will scatter and reflect more NIR radiation, which is unusable for photosynthesis. By calculating the difference between bands measuring red and NIR reflectances, NDVI accentuates the particular signature of green vegetation while attenuating undesired influences from non-vegetative elements. NDVI, and other similar indices, have proven effective in assessing chlorophyll content (*4, 5*), being a good proxy of vegetation density parameters, like the leaf area index (LAI) and the fractional vegetation cover (FVC) (*6, 7, 8*),

as well as the fraction of absorbed photosynthetically active radiation (fAPAR). The success of NDVI relies on its ease of use and its availability over long observational records expanding more than three decades, notably thanks to the Advanced Very High Resolution Radiometer (AVHRR), Landsat optical sensors (MSS, TM, ETM, OLI), and the Moderate Resolution Imaging Spectroradiometer (MODIS).

However, NDVI has two major limitations. First, the relationship between NDVI and green biomass is non-linear and saturates. Some indices such as the enhanced vegetation index (EVI) (*9*) have tried to compensate for this using information from other bands, but the saturation problem still remains. Other approaches have tried to improve NDVI heuristically to obtain a good proxy of both fAPAR and light-use efficiency (LUE), and hence suggested it for gross primary productivity (GPP) estimation (*10*). Actually, some authors have proposed $NDVI^2$ (*11*) and other arbitrary exponentiations (*12*) to cope with the nonlinear issue. The second issue is that VIs, by construction, react to the presence of green leaves, but not to photosynthesis *per se*. GPP can thus decline without any leaf abscission (i.e. a reduction of LAI) or reduction in chlorophyll. A relatively new way to estimate GPP variability from satellite measurements is retrieving sun-induced chlorophyll fluorescence (SIF) (*13*). However, the relationship between canopy GPP and SIF retrieved from space is still not fully understood (*14*), and more importantly, this technique is still only available with an overly coarse spatial resolution and a very shallow temporal archive (*15, 16*).

Using radiative transfer models, Sellers et al. (*17, 18, 19*) noted early on that NIR reflectance is a better proxy for fAPAR than NDVI. And the problem is then to disentangle the fraction of the NIR that is reflected from the vegetation from the remaining fraction of NIR reflected from non-vegetated elements within a mixed pixel. To address this issue, Badgley et al. (*20*) proposed considering NDVI as a proxy for vegetation coverage instead of a proxy for fAPAR, and thus multiply NDVI times NIR to calculate a new index, NIRv, which shows high correlations with SIF and GPP at specific temporal scales. Despite its wide reception in the community, NIRv also raises some intriguing questions. For example, given that fAPAR is estimated by both of its components (NIR and NDVI), how does this affect the interpretation of the index? Also, as NIRv linearly scales with the NIR reflectance, how does it deal with saturation? Finally, NIRv still uses the same bands as NDVI, but it is neither clear how the adopted approximations and assumptions impact NIRv nor whether it exploits all available information in these spectral bands.

This paper introduces a methodology to generalize the broad family of vegetation indices based on differences and ratios of spectral bands. Unlike previous approaches to improve indices based on principled (*21, 20, 10*) or heuristic parametric transformations (*22, 23, 12, 11*), here we adopt a machine learning standpoint using the theory of kernel methods, which has been widely used to derive nonlinear algorithms from linear ones, while still resorting to linear algebra operations (*24,25*). Kernel methods map the involved spectral bands using a nonlinear feature map to a higher dimensional space where the index is defined. Interestingly, the calculation can be expressed in terms of the spectral channels by the definition of a kernel (similarity) function, so one does not need to define the feature map explicitly. The main property of kernel methods is that of *linearizing* the problem, which is what

most of the indices seek either heuristically or based on first principles. Also, by using a particular kernel function, we have guarantees that *all* higher order relations between the spectral channels are accounted for, not just the first order ones. For example, when using differences between near-infrared and the red bands, the kernel function summarizes all monomials of the differences too, i.e. $\{$NIR-red, (NIR-red)^2, (NIR-red)^3, $\ldots\}$ in a single scalar. Although kernel methods can, in principle, be applied to any vegetation index (see S1.5, and Table S1), the framework is illustrated here to generalize NDVI, largely because of the long history and wide utility of this index, most notably to perform global and long-term studies. We specifically define the NDVI in Hilbert spaces, and adopt the radial basis function (RBF) reproducing kernel, k(NIR,red) = $\exp(-\frac{1}{2\sigma^2}(\text{NIR-red})^2)$, where the σ parameter controls the notion of distance between the NIR and red bands. The presented kernel NDVI (kNDVI) reduces to compute

$$\text{kNDVI} = \tanh\left(\left(\frac{\text{NIR-red}}{2\sigma}\right)^2\right),$$

where σ is a lengthscale parameter to be specified in each particular application and represents the sensitivity of the index to sparsely/densely vegetated regions. A reasonable choice is taking the average value $\sigma = 0.5$(NIR+red) (see S1 and S2 for mathematical and ecophysiological justifications), which leads to a simplified operational index version expressed as kNDVI $= \tanh(\text{NDVI}^2)$. The selection of the kernel function and prescription of its parameter allows the kNDVI to perform an automatic and pixel-wise adaptive stretching, and guarantees that all moments of the relations between the NIR and red channels are taken into account. This also allows kNDVI to cope with saturation effects, complex phenological cycles and seasonal variations, to deal with the mixed-pixel problem (*20*), and to propagate lower uncertainty than other indices (S2.5). It can be shown that kNDVI actually generalizes NDVI and NIRv theoretically (see S1, S2 and Properties S2.1-S2.2), which ensures an improved performance. Finally, the presented methodology, and the kNDVI in particular, are easy to implement and use in practice (S10), which is of paramount relevance in operational studies.

Results and discussion

We show that kNDVI exhibits consistently stronger correlations than NDVI and NIRv in key independent products (GPP at flux tower estimates and SIF from GOME-2). In general, the proposed index performs better than NDVI and NIRv in all applications, biomes, and climatic zones. The kNDVI is more resistant to saturation, bias, and complex phenological cycles, and shows enhanced robustness to noise, and stability across spatial and temporal scales (S6.2, S6.3). Additional results for approximating MODIS LAI (S4), correlation with other related parameters (like fAPAR and FVC) acquired *in situ* (S7), crop yield estimation (S8), and kNDVI's use for image change detection (S9) further confirms the validity of the approach. All this without any specific assumption, just statistics.

Accurate proxy to gross primary production

We evaluated and compared the performance of kNDVI with NDVI and NIRv as a GPP proxy using flux tower GPP estimates from the FLUXNET database (S5). The proposed kNDVI provides similar or better correlations with GPP than the other indices over all considered biomes and across all the 169 flux tower sites (Table 1). The weakest relationships are observed for evergreen broad-leaved forests, which can be expected due to the stronger saturation effect in such ecosystem (similarly clear when using the index for LAI estimation, see S4). The kNDVI excels in each biome individually, confirming its adaptive nature, and globally shows a clear gain (Fig. 1). Although photosynthesis is driven by the amount of vegetation photosynthetic mass within a pixel, solar irradiation and environmental constraints also play a critical role. The latter is not accounted for by the spectral information provided by NIR and red bands. This explains why all indices present lower correlation with GPP and SIF than with LAI for all biomes (Table 1, cf. S4). The correlation is however higher for the kNDVI in almost all cases. Alternative measures of nonlinear association between GPP and the indices, like Spearman's correlation (*26*), mutual information (*27*) and distance correlation (*28*) yielded similar results and conclusions, see S5 and S6, thus confirming the good capabilities of kNDVI to implicitly linearize the problem.

We studied the robustness of the indices across sites. Figure 2 shows the density and boxplots of the slopes (scaled between 0 and 1) for all 169 flux tower sites. The NIRv index shows a mean closer to 0.5, but the spread is higher than for the kNDVI. Both NDVI and NIRv show very wide whiskers (and hence pathological behaviours and high sensitivity to outliers), while kNDVI shows higher robustness and stability across sites. A simple analysis over all the towers shows that kNDVI outperformed in 84 of the towers (50%), NIRv in 59 (35%), and NDVI in 26 (15%). The kNDVI gains are more noticeable in deciduous and evergreen forests, which confirms the good adaptation to varying photosynthetic phenology of different biomes, primarily forests. This is confirmed when looking at the seasonal patterns of stand photosynthesis for some illustrative sites in Fig. 3, expressed as monthly GPP. For example, the CA-TP4 (Ontario - Turkey Point 1939 Plantation White Pine site) is a region dominated by densely covered woody vegetation and displays green foliage all year round. Unlike NDVI that shows relatively too much and too little sensitivity respectively to seasonally changing GPP, the kNDVI follows much better the temporal shape and captures the higher and lower GPP values too. This might be due to the subtle pigment shifts that are largely invisible to NDVI, but may be more detectable by kNDVI, as it was recently shown with NIRv (*29*). For grasslands, like the CH-Oe1 (Oensingen, Switzerland), neither NDVI nor NIRv can disentangle the phenological cycle of the vegetation from the background noise, while the kNDVI returns acceptable results with larger dynamic range. Here the tree and shrub cover is less than 10% and a permanent mixture of water and herbaceous or woody vegetation is observed, inducing a strong mixed-pixel problem aggravated by complex topography. The IT-Ro1 (Roccarespampani-1 near Viterbo site) is a deciduous broad-leaved forest consisting of broadleaf tree communities with a clear annual cycle of long leaf-on and leaf-off periods, which are followed faithfully by the kNDVI index. Interestingly NIRv and

kNDVI reveal very similar characteristics. An interesting case is that of closed shrublands. The mixed shrub foliage in the Kennedy Space Center site CSH US-KS2, which can be either evergreen or deciduous, is efficiently handled by kNDVI ($R = 0.72$) over NIRv ($R = 0.68$) and NDVI ($R = 0.57$). Here, unlike NIRv, the proposed kNDVI does not over and underestimate GPP. Overall, we observed that the kNDVI closely tracked the seasonal dynamics of photosynthesis, presenting a better agreement with GPP. This is achieved by adaptively stretching the dynamic range to better capture time-series extremes (e.g. sparsely and densely vegetated, as well as cold and dry regions). The proposed kNDVI seems to largely correct for "background effects" (important in sparse vegetation or snow) and saturation, and may be more sensitive to subtle greenness shifts (e.g. evergreens) based on pigments rather than structure *per se*.

Closer monitoring of photosynthetic activity of ecosystems

Recent studies have linked SIF and vegetation indices, such as NDVI and NIRv (*20*), as a pragmatic alternative to more sophisticated machine learning approaches (*30*). We here evaluate the kNDVI computed from the MODIS reflectance bands to approximate globally gridded GOME-2 SIF at 16-daily resolution. Despite the fact that GOME-2 can measure both SIF and the NIR and red bands simultaneously, we intentionally estimated all indices independently from coincident MODIS data (see processing details in S6). We computed the correlation between time series. The kNDVI outperforms the other indices in general (Fig. 1) and in all biomes individually (Table 1), especially in DBF, GRA, and CRO: 5-11% gain in correlation over NIRv and 20-35% over NDVI.

To confirm the robustness to capture extreme SIF values, we studied the spatial maps of temporal correlation coefficients. kNDVI dominates in all regions, Fig. 4[top], and correlates better with SIF in 69.69% of the pixels compared to NIRv and in 91.32% of cases compared to NDVI, see Fig. 4[bottom]. Results suggest that the kNDVI clearly outperforms the other indices in densely vegetated tropical (e.g. Amazonia, Indonesia) as well as arid regions (e.g. Australia, Mediterranean). As for the case of GPP, other measures of correlation yielded identical conclusions (Table S7). Further analysis confirmed the dominant performance of kNDVI in all latitudes, especially in higher and lower ones (Table S10), as well as in all climatic zones, especially in the arid and cold regions (Table S9).

The study areas in Fig. 4 showed the biggest differences between the kNDVI and NDVI and NIRv, and are further scrutinized in Fig. 5. The kNDVI provides improved fit scores in all cases, larger excursions in general, and more resistance to noise and saturation. The higher accuracy by kNDVI (e.g. in California, +19% in R over NIRv) comes mainly from the better behaviour in the presence of sharp phenological cycles. Interestingly, in the Iberian peninsula, kNDVI and NIRv perform similarly in quantitative terms, but the proposed kNDVI appears less affected by high frequency components and covers the whole dynamic range nicely. In Australia, the favourable numerical gain in R (+25%) and the much lower scatter highlight that kNDVI better approximates SIF, and closely follows the cycles (especially in MAM periods). Despite the big challenges in the Amazon for SIF estimation with GOME-2, the kNDVI can be a more convenient choice compared to other indices, as it deals

better with noise and background effects (e.g. soil, standing water, or snow). All in all, the proposed kNDVI seems better qualified to cope with noise, saturation and complex phenologies.

Similar conclusions were obtained when we studied spatial correlations through time: the proposed index achieves noticeable improvements over NDVI and NIRv, especially between August-November thus improving autumn phenology due to its adaptive stretching (see Fig. S10 in S6). The kNDVI is more competitive at finer temporal resolutions (native biweekly) with a noticeable advantage over NDVI (+15%) and NIRv (+4%), but the gain over NIRv disappears at bimonthly scales, since the temporal aggregation induces a 'more linear' problem. Likewise, a broader spatial aggregation (from 0.5 up to 2) yielded improved results of all indices, but kNDVI still outperformed the others independently of the spatial scale (S6 and Fig. S11).

We finally studied the capabilities of kNDVI to deal with the mixed-pixel problem (Fig. 6). Both kNDVI and NIRv scale with the total NIR, NIR_T, unlike NDVI that clearly saturates. The kNDVI strongly correlates with SIF over highly vegetated pixels, but the correlation decreases with lower vegetated fractions (Fig. 6). The difference between kNDVI and NDVI stands out, and kNDVI is slightly higher correlated with SIF than NIRv, thus suggesting that the index can reliably isolate the proportion of reflectance attributable to vegetation as well. Importantly, these properties emerge directly from the NIR-red relations since no assumption is made in designing the index. Accounting for all NIR-red relations allows to optimally disentangle the mixed-pixel problem efficiently, especially in the densely vegetated areas (e.g LAI and GPP phenology of crops in S4 and Fig. 3).

Conclusions

The study of natural and agricultural systems should greatly benefit from the kNDVI proposed here due to its solid theoretical foundation combined with its ease of calculation and application. The high correlation with GPP and SIF across all biomes, especially in grasslands, croplands and mixed forests as well as in arid regions, suggest that the index can efficiently cope with both the saturation and the mixed-pixel problems encountered with traditional indices. The proposed kNDVI explains a large fraction of the variance of GPP at flux tower level, showed good robustness capabilities to noise and saturation, and enhanced stability across space. The kNDVI also highly correlates with SIF derived from an independent sensor, paving the way toward improving our quantification and understanding of photosynthesis at the global scale. Its application and usefulness goes beyond vegetation monitoring, and embraces change and extreme detection, phenological and greening studies, upscaling parameters, and all applications where vegetation indices in general and NDVI in particular have previously demonstrated their utility. Our results demonstrate that an agnostic statistical approach is sufficient to explain most of the observed signal.

The kernel methods framework allowed us to generalize all vegetation indices, but we focused on the NDVI case only. Kernel methods in general, and the kNDVI in particular, implement the original operation (e.g. NDVI) in a high-dimensional feature space where spectral bands are mapped to. The solution of kNDVI is thus a nonlinear version of NDVI. The framework allows us to accomplish the

ever-sought linearization operation implicitly. This means that no *ad hoc* parametric transformations are needed, just the kernel operation. This also implies that virtually no gain should be obtained over other indices when the relation between the bands and the parameter of interest is linear, such as for instance when an appropriate PAR normalization is applied (see S5.2 and S6.4) or whenever one averages over larger spatial or temporal scales (see S6.3). Our results however suggested that the kNDVI instantiation improved results in all problems, even when the domain was previously linearized. This makes the index a very powerful and practical default choice. We anticipate a wide use and development of the proposed index in particular, and of the family of nonlinear vegetation indices in general, to derive informative indicators for operational Earth monitoring and the quantification of the terrestrial biosphere vital signs.

Materials and Methods

Data sets and processing

GPP and FLUXNET data

The GPP data were obtained from FLUXNET, which is a collection of sites from multiple regional networks (*31*). This network provides a compilation of *in situ* observations to measure the exchanges of carbon dioxide, water vapor, and energy between the biosphere and atmosphere (*32*). To calculate the GPP, the carbon dioxide flux, i.e. net ecosystem exchange (NEE), is measured by means of the eddy covariance method. This flux is further partitioned into ecosystem respiration and GPP [gC/m^2/d] using the daytime (*33*) or nighttime (*34*) partitioning methods. For our analyses, we used GPP estimates from the freely available Tier-1 data set that were obtained with the daytime partitioning method. Of all available sites (212), we selected a subset of 169 sites corresponding with natural vegetation having less than 50% of missing remotely sensed data due to cloud contamination. In addition, we only considered sites where we had more than four months of available flux data.

SIF data from GOME-2

We generated GOME-2 0.5 fluorescence at 740 nm, and reflectance at 670 and 780 nm from level 2 data obtained from measurements of the Global Ozone Monitoring Experiment-2 (GOME-2) sensor flying onboard MetOp-A. The retrieval algorithm of SIF [mW/m^2/sr/nm] proposed in (*35*) uses the filling-in of Fraunhofer lines caused by the plants' chlorophyll fluorescence. Data were gridded to 16 daily and 0.5^o resolutions from the individual soundings, and cover 11 years (2007-2017). No spatial smoothing or temporal averaging was performed before computing or averaging results. High sun zenith angle (SZA) observations (SZA$>$70) deg were removed from the analysis as well as cloudy scenes with a cloud fraction over 50% and observations taken between 2 pm and 8 am local time. The illumination corrected SIF/cos(SZA) was considered, cf. S6.

MODIS BRDF-corrected reflectances

MODIS reflectance data were derived from the MCD43A4.006 BRDF-Adjusted Reflectance 16-Day L3 Global 500m product (*36*). They are disseminated from the Land Processes Distributed Active Archive Center (LP DAAC) also available at Google Earth Engine (GEE). The MCD43A2 MODIS product, which contains ancillary quality information for the corresponding MCD43A4 product, was also used for avoiding low-quality BRDF estimates. We computed the indices and conducted the analysis at 16-day temporal and 500-m spatial scales over the 11 years of SIF data.

Analysis

General rationale

In all our experiments we used reflectance values from MODIS, yet radiances or digital counts could be also used. The flux tower GPP estimates in our experiments come from the site-level data in (*37*). The SIF product comes from GOME-2 so the product is fully independent of MODIS reflectances. GPP and SIF correlations are computed in the time domain, while for SIF we additionally compute correlations in space and then average results over time (results shown in S6).

In all cases we compute correlations between indices (NDVI, NIRv and kNDVI) and the considered product only in meaningful vegetation classes: Needleleaf Forest, Evergreen Broadleaf Forest, Decidious Broadleaf Forest, Mixed forest, Shrublands, Savannas, Herbaceous, and Cultivated. These resulted from a meaningful grouping of IGBP classes (see S3). Analysis of the SIF results also considered aggregated climatic zones (Tropical, Arid, Temperate, Cold, and Polar), monthly means, and latitude averages, see S6.

kNDVI calculation

The kNDVI index is defined as

$$\text{kNDVI} = \frac{k(n,n) - k(n,r)}{k(n,n) + k(n,r)}, \tag{1}$$

where $n, r \in \mathbb{R}$ refer to the reflectances in the NIR and red channels, respectively, and the kernel function k measures the similarity between these two bands. We used in all cases the Radial Basis Function (RBF) kernel, $k(a,b) = \exp(-(a-b)^2/((2\sigma^2))$, where the σ parameter controls the notion of distance between the NIR and red bands. This kernel function induces an important simplification:

$$\text{kNDVI} := \frac{1 - k(n,r)}{1 + k(n,r)} = \tanh\left(\left(\frac{n-r}{2\sigma}\right)^2\right). \tag{2}$$

Other kernel functions are possible but the RBF kernel is the most widely used one because of its theoretical and practical advantages (*24, 25*) (see S1, S2). We calculated the kNDVI fixing the length-scale parameter σ equal to the mean distance between the near-infrared and red bands, $\sigma = 0.5(n+r)$,

which is a standard heuristic in the kernel methods literature, makes the index adaptive to each pixel, and worked very well in practice. Note that this simplification further reduces the index to

$$\mathrm{kNDVI} = \tanh(\mathrm{NDVI}^2). \tag{3}$$

Further optimization of σ per biome was done but results did not improve substantially (results not shown).

Reproducibility: Open-source software and data

All calculations, visualization and analyses were performed using the MATLAB programming language. We stored and processed netCDF files and tabular data. The kNDVI can be easily coded and applied. We give implementations in five standard programming languages (MATLAB, R, Python, Julia, IDL) and in the Google Earth Engine (GEE) in S10.

Supplementary materials

Fig. S1. Spatial distribution of the kernel parameter σ
Fig. S2. Correlation coefficient between SIF and the indices
Fig. S3. Derivative (sensitivity) of kNDVI and NIRv with respect NDVI
Fig. S4. Density of the propagated errors by all indices
Fig. S5. Location of the BELMANIP2.1 sites and associated biomes
Fig. S6. Averaged correlations between LAI and the indices
Fig. S7. Correlation coefficient between LAI and the indices
Fig. S8. Time series over a cultivated and herbaceous areas
Fig. S9. Averaged correlations between GPP and indices per biome type
Fig. S10. Monthly/seasonal correlations between the index and SIF per biome and season
Fig. S11. Correlation between SIF and indices at different spatial and temporal scales
Fig. S12. RGB composite images used for change detection experiments
Fig. S13. Results of the change detection experiments

Table S1. Examples of vegetation indices and their kernel versions
Table S2. IGBP classification
Table S3. Considered IGBP classes and their grouping in our study
Table S4. Correlation between the vegetation indices and LAI per biome
Table S5. Dependence measures of GPP and indices with/without PAR normalization
Table S6. Spatial correlation coefficients between indices and SIF per biome
Table S7. Dependence measures of SIF and indices with/without PAR normalization
Table S8. Temporal correlation between SIF and indices with/without normalization per biome
Table S9. Temporal correlation between SIF and indices with/without normalization per climate zone
Table S10. Temporal correlation between SIF and indices with/without normalization per latitude
Table S11. Dependence measures between indices and in-situ biophysical parameters
Table S12. Correlation coefficients in crop yield estimation
Table S13. Quantitative assessment of errors in crop yield estimation

References

1. J. Xue, B. Su, Significant remote sensing vegetation indices: A review of developments and applications. *Journal of Sensors* **2017**, 1-17 (2017).

2. J. Rouse Jr, R. Haas, J. Schell, D. Deering, Monitoring vegetation systems in the great plains with ERTS (1974).

3. C. Tucker, Red and photographic infrared linear combinations for monitoring vegetation. *Rem. Sens. Environ.* **8**, 127-150 (1979).

4. R. B. Myneni, F. G. Hall, P. J. Sellers, A. L. Marshak, Interpretation of spectral vegetation indexes. *IEEE Trans. Geosc. Rem. Sens.* **33**, 481-486 (1995).

5. D. Haboudane, J. R. Miller, E. Pattey, P. J. Zarco-Tejada, I. B. Strachan, Hyperspectral vegetation indices and novel algorithms for predicting green LAI of crop canopies: Modeling and validation in the context of precision agriculture. *Rem. Sens. Environ.* **90**, 337-352 (2004).

6. G. Le Maire, C. Francois, K. Soudani, D. Berveiller, J. Y. Pontailler, N. Breda, H. Genet, H. Davi, E. Dufrane, Calibration and validation of hyperspectral indices for the estimation of broadleaved forest leaf chlorophyll content, leaf mass per area, leaf area index and leaf canopy biomass. *Rem. Sens. Environ.* **112**, 3846-3864 (2008).

7. D. Haboudane, N. Tremblay, J. Miller, P. Vigneault, Remote estimation of crop chlorophyll content using spectral indices derived from hyperspectral data. *IEEE Trans. Geosc. Rem. Sens.* **46**, 423-436 (2008).

8. J. Berni, P. Zarco-Tejada, L. Suárez, E. Fereres, Thermal and narrowband multispectral remote sensing for vegetation monitoring from an unmanned aerial vehicle. *IEEE Trans. Geosc. Rem. Sens.* **47**, 722738 (2009).

9. A. Huete, K. Didan, T. Miura, E. Rodriguez, X. Gao, L. Ferreira, Overview of the radiometric and biophysical performance of the MODIS vegetation indices. *Remote Sensing of Environment* **83**, 195 - 213 (2002).

10. J. Joiner, Y. Yoshida, Y. Zhang, G. Duveiller, M. Jung, A. Lyapustin, Y. Wang, C. J. Tucker, Estimation of terrestrial global gross primary production (GPP) with satellite data-driven models and eddy covariance flux data. *Remote Sensing* **10**, 1346 (2018).

11. S. Wang, L. Zhang, C. Huang, N. Qiao, An NDVI-Based Vegetation Phenology Is Improved to be More Consistent with Photosynthesis Dynamics through Applying a Light Use Efficiency Model over Boreal High-Latitude Forests. *Remote Sensing* **9**, 695 (2017).

12. W. Wu, The generalized difference vegetation index (GDVI) for dryland characterization. *Remote Sensing* **6**, 1211–1233 (2014).

13. Y. Ryu, J. A. Berry, D. D. Baldocchi, What is global photosynthesis? History, uncertainties and opportunities. *Remote sensing of environment* **223**, 95–114 (2019).

14. A. Porcar-Castell, E. Tyystjärvi, J. Atherton, C. Van der Tol, J. Flexas, E. E. Pfündel, J. Moreno, C. Frankenberg, J. A. Berry, Linking chlorophyll a fluorescence to photosynthesis for remote sensing applications: mechanisms and challenges. *Journal of experimental botany* **65**, 4065–4095 (2014).

15. G. Duveiller, F. Filipponi, S. Walther, P. Köhler, C. Frankenberg, L. Guanter, A. Cescatti, A spatially downscaled sun-induced fluorescence global product for enhanced monitoring of vegetation productivity. *Earth Syst. Sci. Data Discuss.* **2019**, 1–24 (2019).

16. J. Wen, P. Köhler, G. Duveiller, N. Parazoo, T. Magney, G. Hooker, L. Yu, C. Chang, Y. Sun, A framework for harmonizing multiple satellite instruments to generate a long-term global high spatial-resolution solar-induced chlorophyll fluorescence (SIF). *Remote Sensing of Environment* **239**, 111644 (2020).

17. P. J. Sellers, Canopy reflectance, photosynthesis and transpiration. *International journal of remote sensing* **6**, 1335–1372 (1985).

18. P. Sellers, Canopy reflectance, photosynthesis, and transpiration, ii. the role of biophysics in the linearity of their interdependence. *Remote sensing of Environment* **21**, 143–183 (1987).

19. P. Sellers, J. Berry, G. Collatz, C. Field, F. Hall, Canopy reflectance, photosynthesis, and transpiration. iii. a reanalysis using improved leaf models and a new canopy integration scheme. *Remote sensing of environment* **42**, 187–216 (1992).

20. G. Badgley, C. Field, J. Berry, Canopy near-infrared reflectance and terrestrial photosynthesis. *Science Advances* **3**, e1602244 (2017).

21. J. A. Gamon, K. F. Huemmrich, C. Y. S. Wong, I. Ensminger, S. Garrity, D. Y. Hollinger, A. Noormets, J. Peñuelas, A remotely sensed pigment index reveals photosynthetic phenology in evergreen conifers. *Proceedings of the National Academy of Sciences* **113**, 13087–13092 (2016).

22. J. Clevers, The derivation of a simplified reflectance model for the estimation of leaf area index. *Remote Sensing of Environment* **25**, 53–69 (1988).

23. P. Gong, R. Pu, G. S. Biging, M. R. Larrieu, Estimation of forest leaf area index using vegetation indices derived from hyperion hyperspectral data. *IEEE transactions on geoscience and remote sensing* **41**, 1355–1362 (2003).

24. G. Camps-Valls, L. Bruzzone, eds., *Kernel methods for Remote Sensing Data Analysis* (Wiley & Sons, UK, 2009).

25. J. Rojo-Álvarez, M. Martínez-Ramón, J. Muñoz-Marí, G. Camps-Valls, eds., *Digital Signal Processing with Kernel Methods* (Wiley & Sons, UK, 2018).

26. M. Hollander, D. A. Wolfe, E. Chicken, *Nonparametric statistical methods*, vol. 751 (John Wiley & Sons, 2013).

27. T. M. Cover, J. A. Thomas, *Elements of Information Theory (Wiley Series in Telecommunications and Signal Processing)* (Wiley-Interscience, USA, 2006).

28. G. J. Székely, M. L. Rizzo, N. K. Bakirov, Measuring and testing dependence by correlation of distances. *The Annals of Statistics* **35**, 2769-2794 (2007).

29. C. Y. Wong, P. DOdorico, M. A. Arain, I. Ensminger, Tracking the phenology of photosynthesis using carotenoid-sensitive and near-infrared reflectance vegetation indices in a temperate evergreen and mixed deciduous forest. *New Phytologist* (2020).

30. P. Gentine, S. Alemohammad, Reconstructed solar-induced fluorescence: A machine learning vegetation product based on MODIS surface reflectance to reproduce GOME-2 solar-induced fluorescence. *Geophysical Research Letters* **45**, 3136–3146 (2018).

31. G. Tramontana, M. Jung, G. Camps-Valls, K. Ichii, B. Raduly, M. Reichstein, C. R. Schwalm, M. A. Arain, A. Cescatti, G. Kiely, L. Merbold, P. Serrano-Ortiz, S. Sickert, S. Wolf, D. Papale, Predicting carbon dioxide and energy fluxes across global fluxnet sites with regression algorithms. *Biogeosciences Discussions* **2016**, 1–33 (2016).

32. D. D. Baldocchi, Assessing the eddy covariance technique for evaluating carbon dioxide exchange rates of ecosystems: past, present and future. *Global Change Biology* **9**, 479-492 (2003).

33. G. Lasslop, M. Reichstein, D. Papale, A. Richardson, A. Arneth, A. Barr, P. Stoy, G. Wohlfahrt, Separation of net ecosystem exchange into assimilation and respiration using a light response curve approach: critical issues and global evaluation. *Global Change Biology* **16**, 187–208 (2010).

34. M. Reichstein, E. Falge, D. Baldocchi, D. Papale, M. Aubinet, P. Berbigier, C. Bernhofer, N. Buchmann, T. Gilmanov, A. Granier, T. Grnwald, K. Havrnkov, H. Ilvesniemi, D. Janous, A. Knohl, T. Laurila, A. Lohila, D. Loustau, G. Matteucci, T. Meyers, F. Miglietta, J.-M. Ourcival, J. Pumpanen, S. Rambal, E. Rotenberg, M. Sanz, J. Tenhunen, G. Seufert, F. Vaccari, T. Vesala, D. Yakir, R. Valentini, On the separation of net ecosystem exchange into assimilation and ecosystem respiration: review and improved algorithm. *Global Change Biology* **11**, 1424-1439 (2005).

35. P. Köhler, L. Guanter, J. Joiner, A linear method for the retrieval of sun-induced chlorophyll fluorescence from GOME-2 and SCIAMACHY data. *Atmospheric Measurement Techniques* **8**, 2589–2608 (2015).

36. C. B. Schaaf, F. Gao, A. H. Strahler, W. Lucht, X. Li, T. Tsang, N. C. Strugnell, X. Zhang, Y. Jin, J.-P. Muller, *et al.*, First operational brdf, albedo nadir reflectance products from modis. *Remote sensing of Environment* **83**, 135–148 (2002).

37. G. Tramontana, M. Jung, C. R. Schwalm, K. Ichii, G. Camps-Valls, B. Ráduly, M. Reichstein, M. A. Arain, A. Cescatti, G. Kiely, L. Merbold, P. Serrano-Ortiz, S. Sickert, S. Wolf, D. Papale, Predicting carbon dioxide and energy fluxes across global FLUXNET sites with regression algorithms. *Biogeosciences* **13**, 4291–4313 (2016).

38. J. Shawe-Taylor, N. Cristianini, *Kernel Methods for Pattern Analysis* (Cambridge University Press, 2004).

39. P. Zarco-Tejada, A. Berjn, R. Lpez-Lozano, J. Miller, P. Martn, V. Cachorro, M. Gonzlez, A. de Frutos, Assessing vineyard condition with hyperspectral indices: Leaf and canopy reflectance simulation in a row-structured discontinuous canopy. *Remote Sensing of Environment* **99**, 271 - 287 (2005).

40. R. E. Crippen, Calculating the vegetation index faster. *Remote Sensing of Environment* **34**, 71 - 73 (1990).

41. A. A. Gitelson, Y. J. Kaufman, R. Stark, D. Rundquist, Novel algorithms for remote estimation of vegetation fraction. *Remote Sensing of Environment* **80**, 76 - 87 (2002).

42. J. Delegido, L. Alonso, G. González, J. Moreno, Estimating chlorophyll content of crops from hyperspectral data using a normalized area over reflectance curve (NAOC). *International Journal of Applied Earth Observation and Geoinformation* **12**, 165-174 (2010).

43. Q. Wang, S. Adiku, J. Tenhunen, A. Granier, On the relationship of NDVI with leaf area index in a deciduous forest site. *Remote Sensing of Environment* **94**, 244 - 255 (2005).

44. F. Baret, J. T. Morissette, R. A. Fernandes, J. L. Champeaux, R. B. Myneni, J. Chen, S. Plummer, M. Weiss, C. Bacour, S. Garrigues, *et al.*, Evaluation of the representativeness of networks of sites for the global validation and intercomparison of land biophysical products: Proposition of the CEOS-BELMANIP. *IEEE Transactions on Geoscience and Remote Sensing* **44**, 1794–1803 (2006).

45. K. Yan, T. Park, G. Yan, C. Chen, B. Yang, Z. Liu, R. Nemani, Y. Knyazikhin, R. Myneni, Evaluation of MODIS LAI/FPAR product collection 6. Part 1: Consistency and improvements. *Remote Sensing* **8**, 359 (2016).

46. B. Schölkopf, A. Smola, *Learning with Kernels – Support Vector Machines, Regularization, Optimization and Beyond* (MIT Press Series, Cambridge, MA, USA, 2002).

47. J. L. Monteith, *Symposia of the society for experimental biology* (Cambridge University Press (CUP) Cambridge, 1965), vol. 19, pp. 205–234.

48. W. K. Smith, S. C. Reed, C. C. Cleveland, A. P. Ballantyne, W. R. Anderegg, W. R. Wieder, Y. Y. Liu, S. W. Running, Large divergence of satellite and Earth system model estimates of global terrestrial CO2 fertilization. *Nature Climate Change* **6**, 306–310 (2016).

49. S. W. Running, R. R. Nemani, F. A. Heinsch, M. Zhao, M. Reeves, H. Hashimoto, A continuous satellite-derived measure of global terrestrial primary production. *Bioscience* **54**, 547–560 (2004).

50. Y. Ryu, J. A. Berry, D. D. Baldocchi, What is global photosynthesis? history, uncertainties and opportunities. *Remote sensing of environment* **223**, 95–114 (2019).

51. J. Delegido, J. Verrelst, L. Alonso, J. Moreno, Evaluation of Sentinel-2 red-edge bands for empirical estimation of green LAI and chlorophyll content. *Sensors* **11**, 7063-7081 (2011).

52. J. Delegido, J. Verrelst, C. Meza, J. Rivera, L. Alonso, J. Moreno, A red-edge spectral index for remote sensing estimation of green LAI over agroecosystems. *European Journal of Agronomy* **46**, 42-52 (2013).

53. S. B. Idso, R. D. Jackson, R. J. Reginato, Remote-sensing of crop yields. *Science* **196**, 19–25 (1977).

54. B. Marinkovi, J. Crnobarac, S. Brdar, B. Anti, G. Jaimovi, V. Crnojevi, *Proc. First Int Workshop on Sensing Technologies in Agriculture, Forestry and Environment (BioSense09), Novi Sad, Serbia* (2009), pp. 1–5.

55. S. Fritz, L. See, J. C. L. Bayas, F. Waldner, D. Jacques, I. Becker-Reshef, A. Whitcraft, B. Baruth, R. Bonifacio, J. Crutchfield, F. Rembold, O. Rojas, A. Schucknecht, M. V. der Velde, J. Verdin, B. Wu, N. Yan, L. You, S. Gilliams, S. Mcher, R. Tetrault, I. Moorthy, I. McCallum, A comparison of global agricultural monitoring systems and current gaps. *Agricultural Systems* **168**, 258 - 272 (2019).

56. R. Fieuzal, C. M. Sicre, F. Baup, Estimation of corn yield using multi-temporal optical and radar satellite data and artificial neural networks. *International journal of applied earth observation and geoinformation* **57**, 14–23 (2017).

57. M. Weiss, F. Jacob, G. Duveiller, Remote sensing for agricultural applications: A meta-review. *Remote Sensing of Environment* **236**, 111402 (2020).

58. X. Zhang, M. A. Friedl, C. B. Schaaf, A. H. Strahler, J. C. Hodges, F. Gao, B. C. Reed, A. Huete, Monitoring vegetation phenology using MODIS. *Remote sensing of environment* **84**, 471–475 (2003).

59. M. O. Jones, L. A. Jones, J. S. Kimball, K. C. McDonald, Satellite passive microwave remote sensing for monitoring global land surface phenology. *Remote Sensing of Environment* **115**, 1102–1114 (2011).

60. P. Zhang, B. Anderson, B. Tan, M. Barlow, R. Myneni, *Geoscience and Remote Sensing Symposium (IGARSS), 2010 IEEE International* (IEEE, 2010), pp. 1815–1818.

61. N. A. Quarmby, M. Milnes, T. L. Hindle, N. Silleos, The use of multi-temporal NDVI measurements from AVHRR data for crop yield estimation and prediction. *International Journal of Remote Sensing* **14**, 199–210 (1993).

62. M. Mkhabela, P. Bullock, S. Raj, S. Wang, Y. Yang, Crop yield forecasting on the Canadian Prairies using MODIS NDVI data. *Agricultural and Forest Meteorology* **151**, 385–393 (2011).

63. D. K. Bolton, M. A. Friedl, Forecasting crop yield using remotely sensed vegetation indices and crop phenology metrics. *Agricultural and Forest Meteorology* **173**, 74–84 (2013).

64. Y. Chen, D. Lu, E. Moran, M. Batistella, L. V. Dutra, I. D. Sanches, R. F. B. da Silva, J. Huang, A. J. B. Luiz, M. A. F. de Oliveira, Mapping croplands, cropping patterns, and crop types using MODIS time-series data. *International Journal of Applied Earth Observation and Geoinformation* **69**, 133–147 (2018).

65. A. Kern, Z. Barcza, H. Marjanović, T. Árendás, N. Fodor, P. Bónis, P. Bognr, J. Lichtenberger, Statistical modelling of crop yield in Central Europe using climate data and remote sensing vegetation indices. *Agricultural and Forest Meteorology* **260-261**, 300–320 (2018).

Notes

Acknowledgements: We thank JL Rojo-Álvarez and M. Martínez-Ramón for the many discussions on kernel methods. LA and JV provided critical feedback on our logic. This work used eddy covariance data acquired and shared by the FLUXNET community, including the following networks: AmeriFlux, AfriFlux, AsiaFlux, CarboAfrica, CarboEuropeIP, CarboItaly, CarboMont, ChinaFlux, Fluxnet-Canada, GreenGrass, ICOS, KoFlux, LBA, NECC, OzFlux-TERN, TCOS-Siberia, and USCCC.

Funding: GCV was supported from the European Research Council (ERC) under the ERC Consolidator Grant 2014 project SEDAL (647423). MCT and FJGH are supported by the EUMETSAT Satellite Application Facility on Land Surface Analysis (LSA-SAF). SR research was financially supported by the NASA Earth Observing System MODIS project (grant NNX08AG87A). JAG acknowledges the support of NASA ABoVE award number NNX15AT78A. SW acknowledges funding from the Emmy Noether Programme (GlobFluo project) of the German Research Foundation (GU 1276/1-1) as well as funding the European Union's Horizon 2020 research and innovation program under grant agreement 776186 (CHE project) and agreement 776810 (VERIFY project).

Author Contributions: GCV and MCT conceived and developed the methodology. SW provided harmonized SIF data, MJ provided harmonized GPP data. MCT collected and harmonized the LAI dataset. GCV, AMM and MCT did the experiments and performed the analysis with help from GD, SW, and LG. JMM implemented the index in several languages, including the GEE platform. All authors analyzed the results and contributed to writing of the manuscript.

Competing Interests The authors declare that they have no competing interests.

Data and materials availability: All data needed to evaluate the conclusions in the paper are present in the paper and/or the Supplementary Materials. Additional data related to this paper may be requested from the authors.

Figures and Tables

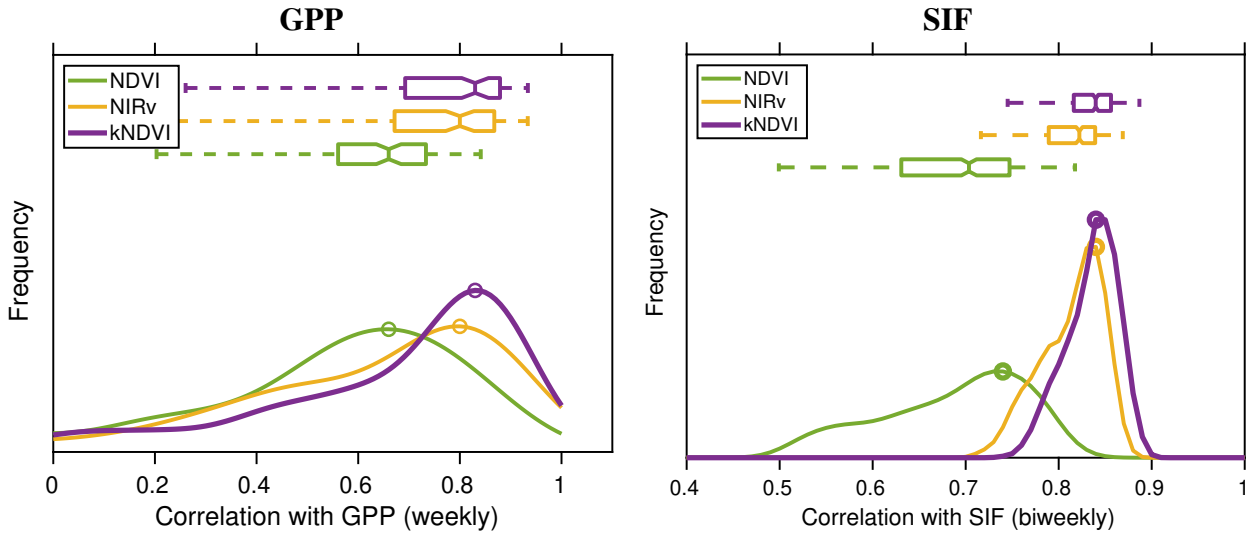

Figure 1: Histogram of the correlation coefficient between the vegetation indices and the parameters: for GPP (left) correlation computed over 169 FLUXNET sites, and for SIF (right) averaged over all 506 global images.

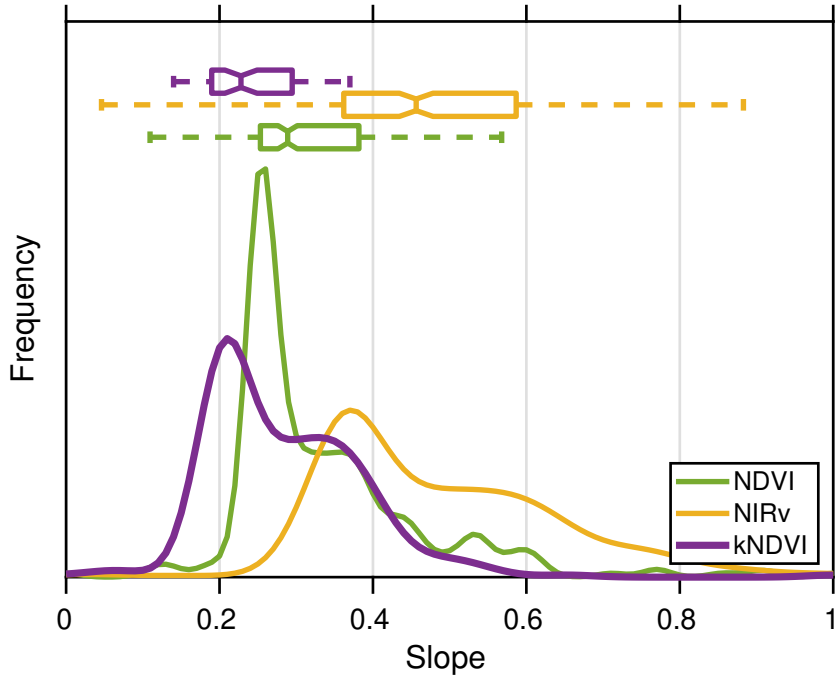

Figure 2: Distribution of slopes of site-level linear regressions (normalized between 0 and 1) between the indices and biweekly GPP from 169 FLUXNET sites.

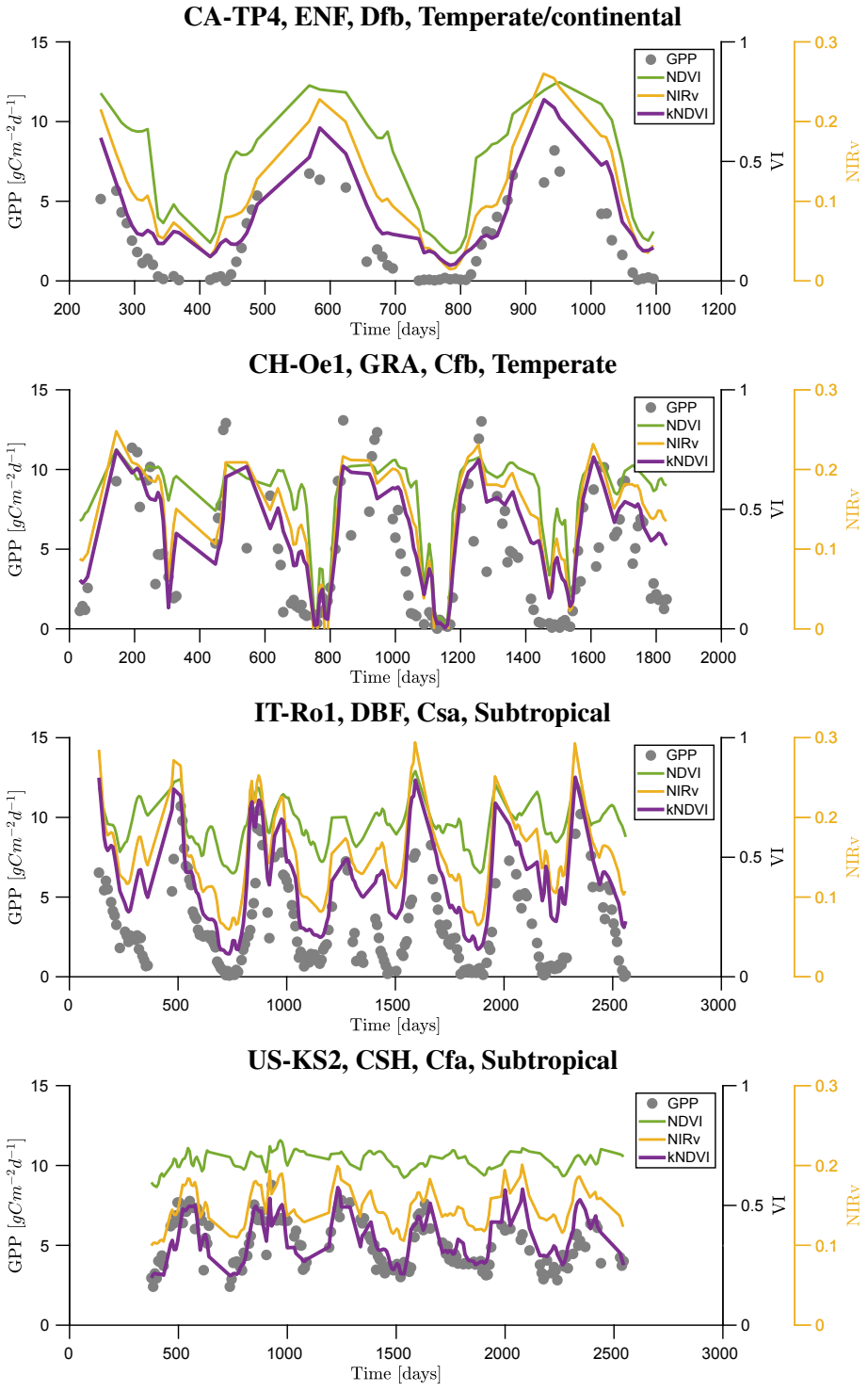

Figure 3: Illustrative results over four flux towers covering evergreen needle-leaved forests (CAT-TP4), grasslands (CH-Oe1), deciduous broadleaf forest (IT-Ro1) and closed shrublands (US-KS2).

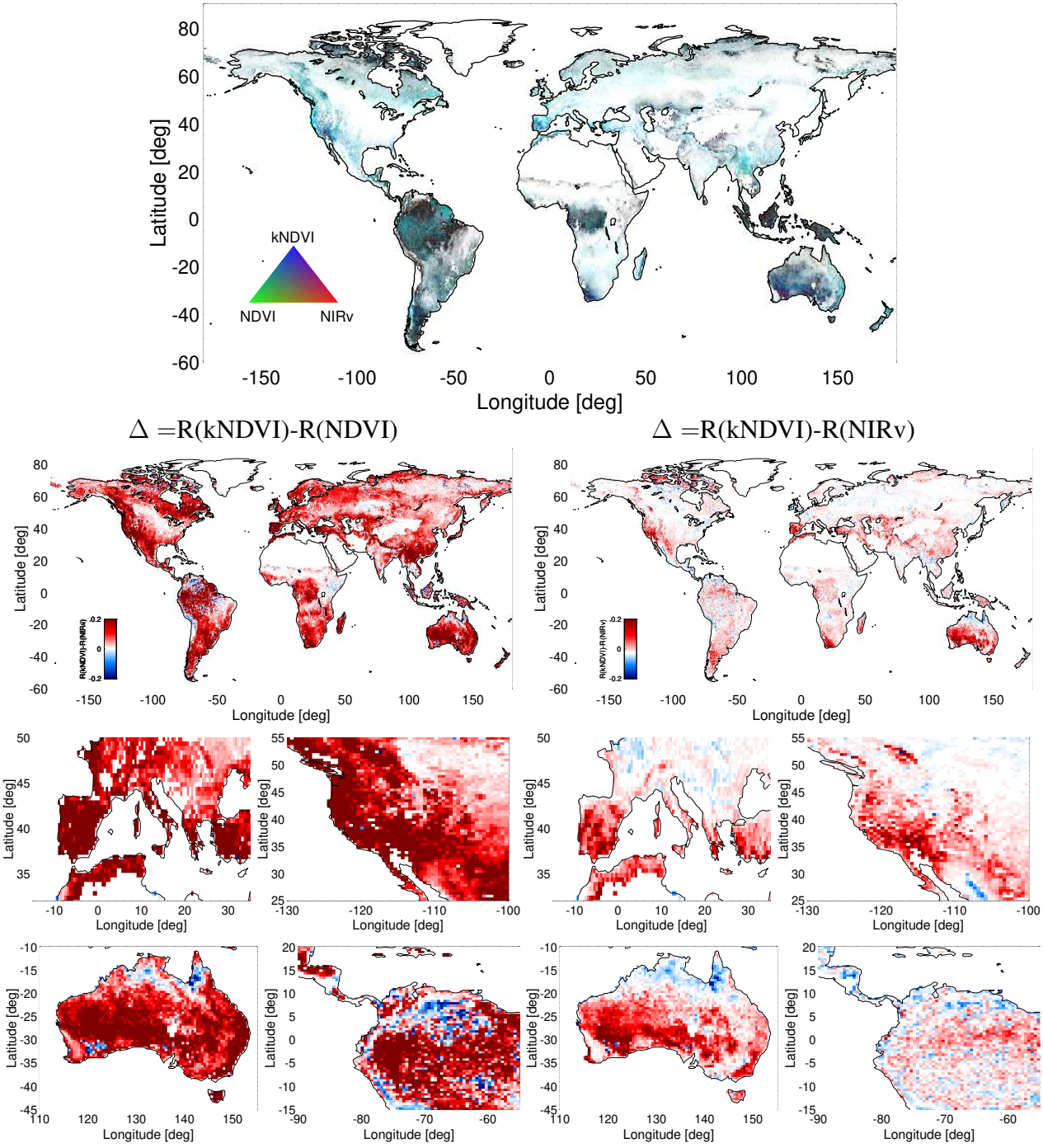

Figure 4: Top: Color composite of indices-to-SIF correlation, (R, G, B) = (NIRv, NDVI, kNDVI). Blueish means kNDVI outperforms the rest, which generally happens (in 91.32% of the pixels over NDVI -left- and 69.69% of the cases over NIRv -right-) and particularly in the extremes (low and high) vegetation covers or in cold and dry regions. Bottom: Differences of correlation-with-SIF between the proposed index kNDVI and NDVI (left) and NIRv (right), both globally and for extreme regions. Red colors indicate a higher correlation for kNDVI and blue indicates a lower correlation for kNDVI (relative to the other indices).

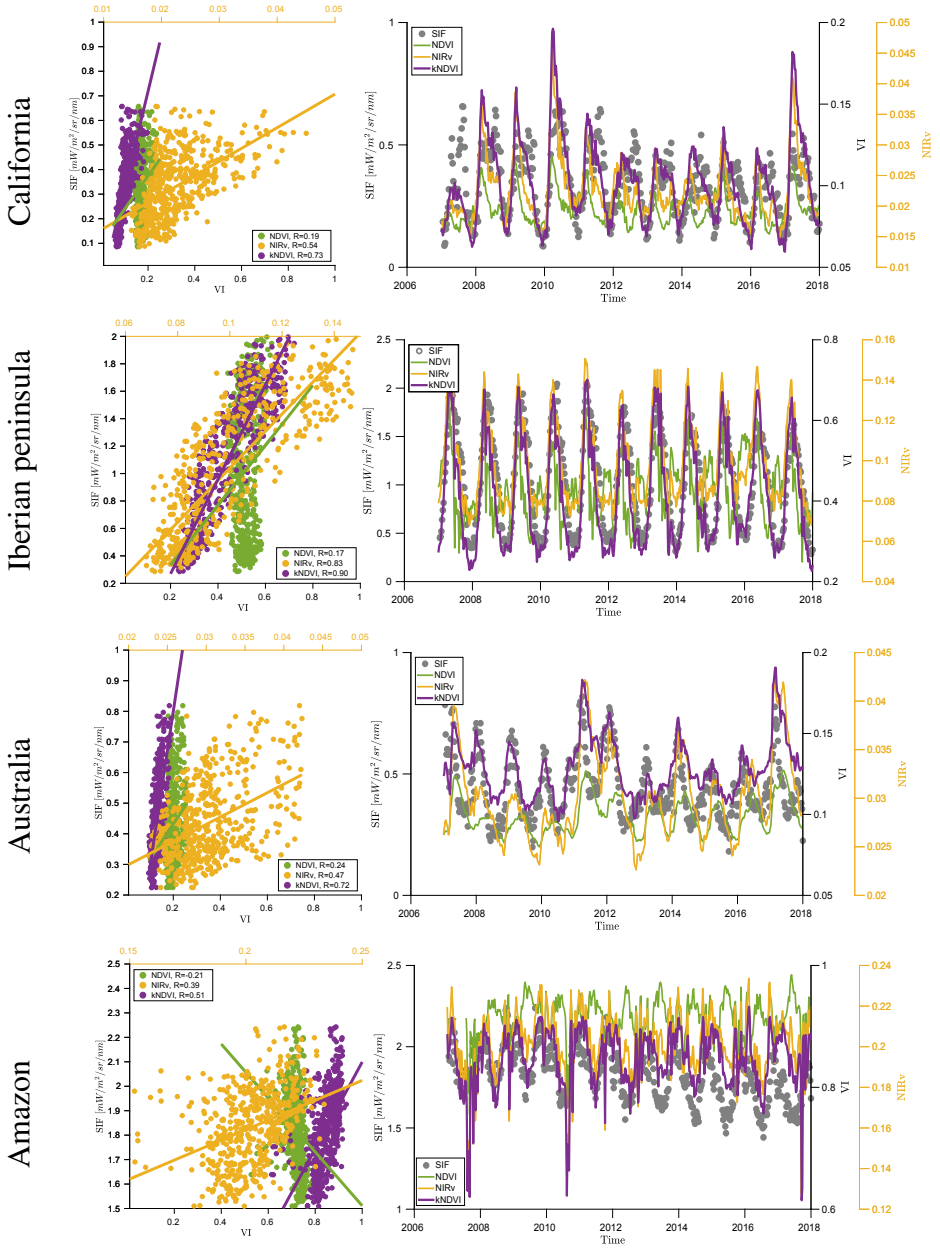

Figure 5: Temporal analysis over selected study areas. Scatter plots of the different indices versus SIF (left), and the average time series over the study areas (right). Axes limits were optimized to improve visualization of all indices.

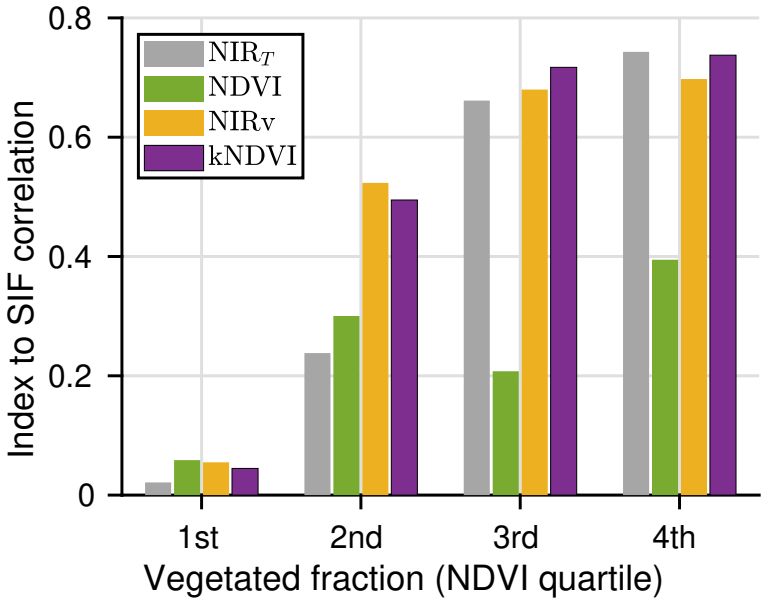

Figure 6: Correlation coefficient between the indices and SIF increases with vegetated fraction (computed from NDVI percentiles). We include the total NIR, NIR$_T$, as a reference. The lower bounds of the NDVI quartiles are as follows: 0, 0.25, 0.50, and 0.75.

Table 1: Temporal correlation coefficient between the vegetation indices and the parameters GPP and SIF per biome. Only vegetation biomes are considered and classes in IGBP were grouped as indicated in parentheses: C1=NF=Needle-leaf Forest (1+3), C2=EBF=Evergreen Broadleaf Forest (2), C3=DBF=Decidious Broadleaf Forest (4), C4=MF=Mixed forest (5), C5=SH=Shrublands (6+7), C6=SAV=Savannas (8+9), C7=GRA=Herbaceous (10), C8=CRO=Cultivated (12). Best results per biome indicated in bold and darker green indicates higher correlation.

		GPP			SIF		
	Biome	**NDVI**	**NIRv**	**kNDVI**	**NDVI**	**NIRv**	**kNDVI**
C1	**NF**	0.59	**0.65**	0.62	0.66	0.73	**0.74**
C2	**EBF**	0.37	**0.45**	**0.45**	0.65	0.72	**0.73**
C3	**DBF**	0.61	0.79	**0.82**	0.41	0.48	**0.51**
C4	**MF**	0.69	0.84	**0.86**	0.61	0.68	**0.70**
C5	**SH**	0.57	0.68	**0.72**	0.63	0.69	**0.71**
C6	**SAV**	0.63	**0.74**	**0.74**	0.56	0.62	**0.63**
C7	**GRA**	0.61	0.71	**0.72**	0.48	0.59	**0.66**
C8	**CRO**	0.51	**0.58**	**0.58**	0.53	0.62	**0.67**
	ALL	0.59	**0.68**	**0.68**	0.54	0.62	**0.65**

Supporting information for the manuscript

"A Unified Vegetation Index for Quantifying the Terrestrial Biosphere"

Contact author: Gustau Camps-Valls, gustau.camps@uv.es
Manuel Campos-Taberner, Álvaro Moreno-Martínez, Sophia Walther, Grégory Duveiller, Alessandro Cescatti, Miguel Mahecha, Jordi Muñoz-Marí, Francisco Javier García-Haro, Luis Guanter, John A. Gamon, Martin Jung, Markus Reichstein, Steven W. Running

Contents

S1 Generalizing Vegetation Indices with Kernels **2**

S2 Mathematical properties of kNDVI **6**

S3 IGBP groups **10**

S4 Correlation with remotely-sensed Leaf Area Index (LAI) **11**

S5 Additional analysis of GPP results **15**

S6 Additional analysis of SIF results **17**

S7 Dependence between the index and in-situ Chlorophyll content, LAI and FVC **21**

S8 Crop yield estimation **22**

S9 Change detection **24**

S10 Source code implementation **25**

S1 Generalizing Vegetation Indices with Kernels

The new family of nonlinear vegetation indices is based on kernel methods (*38, 24*), a machine learning methodology to derive nonlinear algorithms from linear ones while still resorting to linear algebra operations. We first review the main theoretical properties of feature maps and kernel functions. Then we exemplify the framework of kernel-based vegetation indices and illustrate it with the particular case of the NDVI.

S1.1 Feature maps and kernel functions

Deriving nonlinear (kernel) indices requires the definition of a feature mapping $\phi(\cdot)$ to a Hilbert space $\mathcal{H}$ endorsed with the kernel reproducing property.

Definition S1.1 Reproducing kernel Hilbert space (RKHS). *Given a Hilbert space $\mathcal{H}$ with functions over ^{d}, i.e. $f : \mathbb{R}^d \to \mathbb{R}$, the function $k(\cdot,\cdot) : \mathbb{R}^d \times \mathbb{R}^d \to \mathbb{R}$ is called reproducing kernel of $\mathcal{H}$ if $k(x,\cdot) \in \mathcal{H}$, and $\mathcal{H}$ is a RKHS.*

Property S1.1 Properties of Hilbert spaces. *A Hilbert space $\mathcal{H}$ is a space endorsed with an inner product. Let $\mathcal{H}$ be a vector space over . A function $\langle\cdot,\cdot\rangle_{\mathcal{H}} : \mathcal{H} \times \mathcal{H} \mapsto$ is said to be an inner product on $\mathcal{H}$ if: (1) $\langle\alpha_1 f_1 + \alpha_2 f_2, g\rangle_{\mathcal{H}} = \alpha_1\langle f_1, g\rangle_{\mathcal{H}} + \alpha_2\langle f_2, g\rangle_{\mathcal{H}}$; (2) $\langle f, g\rangle_{\mathcal{H}} = \langle g, f\rangle_{\mathcal{H}}$; and (3) $\langle f, f\rangle_{\mathcal{H}} \geq 0$, and $\langle f, f\rangle_{\mathcal{H}} = 0$ iff $f = 0$.*

Property S1.2 Reproducing property. *If $\forall x \in \mathbb{R}^d$ and $\forall f \in \mathcal{H}$ then $f(x) = \langle f, k(x,\cdot)\rangle$ and the product $\langle k(\cdot,x), k(\cdot,z)\rangle_{\mathcal{H}} = k(x,z)$. This is the reproducing property of the kernel. A function f can thus be represented as a linear function defined by an inner product in the vector space $\mathcal{H}$.*

S1.2 An illustrative example: NDVI

The normalized difference vegetation index is defined as NDVI $= \frac{n-r}{n+r}$, where n and r are the reflectances in the NIR and the red bands, respectively. This is a difference-ratio operation: the difference in the numerator can be cast as the 'physical' component, while the sum in the denominator is a 'normalization' factor. For the formulation of the kernel NDVI let us treat the two components separately. Given scalars $n, r \in \mathbb{R}$, $d = 1$, let us define a feature map $\phi \mapsto \phi(n) \in \mathcal{H}$ with an associated reproducing kernel $k(n,\cdot) = \langle\phi(n),\cdot\rangle_{\mathcal{H}}$, likewise for r. Now let us define two feature maps that work on the joint (n, r) feature vector:

$$\psi((n,r)) := \phi(n) - \phi(r) \in \mathcal{H} \quad \textit{and} \quad \varphi((n,r)) := \phi(n) + \phi(r) \in \mathcal{H},$$

with associated physical and normalization kernels:

$$\begin{aligned} m((n,r),(n,r)) &= \langle\psi((n,r)), \psi((n,r))\rangle_{\mathcal{H}} = k(n,n) + k(r,r) - k(n,r) - k(r,n) \\ \ell((n,r),(n,r)) &= \langle\varphi((n,r)), \varphi((n,r))\rangle_{\mathcal{H}} = k(n,n) + k(r,r) + k(n,r) + k(r,n). \end{aligned}$$

We can estimate the kernel NDVI transformation for (n, r) simply as:

$$\text{kNDVI} = \frac{m((n,r),(n,r))}{\ell((n,r),(n,r))} = \frac{k(n,k) - k(n,r)}{k(n,n) + k(n,r)}.$$

Property S1.3 *All kernels in kNDVI are positive definite. By construction ϕ leads to a positive definite kernel k. The difference between feature maps in ψ might not lead to a valid kernel because the third property of kernel functions in S1.1 could be violated because m could be negative in principle. The kernel is however symmetric since $m((n,r),(n,r)) = m((r,n),(r,n))$, and positive by construction, since $\langle \phi(n) - \phi(r), \phi(n) - \phi(r) \rangle_{\mathcal{H}} = \|\phi(n) - \phi(r)\|^2_{\mathcal{H}} \geq 0$. Actually, for the particular case of the RBF kernel function, we have $k(x,x) = 1$, and therefore $m((n,r),(n,r)) = 2(1-k(n,r)) \geq 0$ by construction since $0 \leq k(n,r) \leq 1$. Also note that $m((n,r),(n,r)) = 0$ iff $n = r$ so that $k(n,r) = 1$. Following similar arguments, the summation feature map φ also leads trivially to a positive definite kernel ℓ and $\ell((n,r),(n,r)) = 2(1 + k(n,r)) \geq 0$. In conclusion, all defined feature maps ϕ, ψ and φ need to lead to positive definite kernels k, m and ℓ respectively, and the multiplication (ratio) of kernels is a valid kernel too thus the kNDVI is a valid kernel.*

S1.3 The choice of the kernel function

The core of any kernel method in general, and the kNDVI in particular, is the appropriate definition of the kernel function, $k(a,b)$. Popular examples of valid reproducing kernels are the linear kernel, $k(a,b) = ab$, the polynomial $k(a,b) = (ab+1)^p$, $p \in \mathbb{Z}^+$, and the radial basis function (RBF) kernel, $k(a,b) = \exp(-\frac{1}{2\sigma^2}(a-b)^2)$, $\sigma \in \mathbb{R}^+$.

Property S1.4 NDVI is equivalent to kNDVI with a linear kernel function. *In the linear kernel, the associated RKHS is the space $\mathbb{R}$, and kNDVI trivially reduces to the standard linear NDVI:*

$$\textit{kNDVI} \overset{\textit{lin}}{:=} \frac{n\,n - n\,r}{n\,n + n\,r} = \frac{n-r}{n+r} = \textit{NDVI}.$$

Property S1.5 *Higher moments kernels. In polynomial kernels of degree p, kNDVI effectively only accounts for moments up to order p:*

$$\textit{kNDVI} \overset{\textit{poly}}{:=} \frac{(n\,n)^p - (n\,r)^p}{(n\,n)^p + (n\,r)^p} = \frac{n^p - r^p}{n^p + r^p}.$$

For the Gaussian kernel, the RKHS is of infinite dimension and kNDVI measures higher order spectral dependencies between the reflectances in the NIR and the red channels. In addition, note that for RBF kernel above, self-similarity $k(a,a) = 1$, and thus the kNDVI measure simply reduces to

$$\textit{kNDVI} \overset{\textit{RBF}}{:=} \frac{1 - k(n,r)}{1 + k(n,r)} = \tanh\left(\left(\frac{n-r}{2\sigma}\right)^2\right).$$

S1.4 Prescription and interpretation of the kernel parameter

In kernel methods, setting the kernel parameters is critical and has an important impact in the solution (*25*). We used in all our experiments the RBF and set the lengthscale parameter σ to the average value between NIR and red, $\sigma = 0.5(n + r)$. This prescription of σ is a reasonable choice; note that σ should reflect the notion of similarity between input data (in our case, NIR and red reflectances). It is customary in the kernel methods literature to fix it to the average distance among objects (here the reflectances in NIR and red channels). This choice can be also interpreted as a rough estimation of the pixel's albedo, see Fig. S1: higher σ are automatically selected for bare soils.

Interestingly, by virtue of this approximation, the simplified kNDVI is a convenient double non-linear transformation of NDVI as it reduces to kNDVI $= \tanh(\text{NDVI}^2)$. First NDVI is squared, and then the result is squashed with a sigmoid function. On the one hand, the squared NDVI has been proposed in (*11*) as a proxy of fAPAR times LUE, and hence very useful to estimate GPP. On the other hand, the $\tanh$ function allows to improve sensitivity at high values, such as in managed croplands, and reduce the well-known bias of NDVI at low values, where photosynthetic activity is low or non-existent.

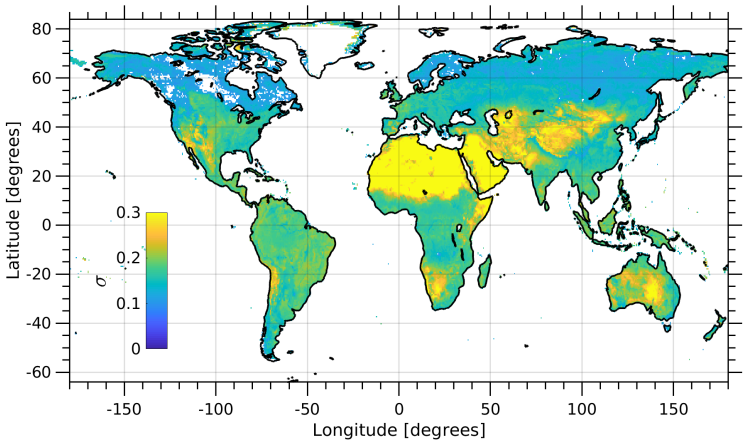

Figure S1: Distribution of the kernel parameter σ computed as the average of NIR and red, $\sigma = 0.5(n + r)$ over the 506 MODIS images (2007-2017) used in the SIF experiment.

The parameter σ directly affects the nonlinearity and may have a strong impact on the index performance. In our experiments, however, we used the mean heuristic that worked very well. Actually, optimizing σ per biome or climatic region to approximate GPP, LAI pr SIF did not improve the results much over the proposed heuristic (results not shown). The reason is that the index is already pixel-adapted. The different σ value per pixel endorses the kNDVI with a high degree of adaptation to dynamic ranges, thus resolving challenging cases of arid, dry, densely and sparsely vegetated regions. The prescribed parameter stretches the predictions to account for high dynamic ranges (e.g for GPP estimation in Fig. 3 and for LAI in Fig. S8), while reducing bias and saturation problems. This behaviour is explained by looking at the sensitivity of the index to NDVI, see S2 and Fig. S3. The suggested $\sigma = 0.5(n + r)$ actually leads to virtually no sensitivity to sparsely vegetated regions (low NDVI, avoiding the bias problem), that varies roughly linearly with NDVI for mixed-pixels (moderate NDVI) and that decreases for highly vegetated regions (high NDVI, reducing the NDVI saturation problem). This, in turn, has a positive effect in terms of error propagation, see S2.5.

S1.5 Generalizing standard vegetation indices with kernel methods

The kernel methodology can be readily applied to any vegetation index available in the literature, provided that it can be expressed as a function of dot products between spectral channels. Table S1 shows some illustrative examples of kernelized indices.

Firstly, one has then to select an appropriate kernel function k (e.g. linear, polynomial, or RBF). We recommend the Gaussian kernel -RBF kernel- function because it captures all higher-order relations between the spectral channels involved, it only contains one hyperparameter to choose, and generally gives good results in many applications. Secondly, one has to choose, or optimize, the kernel parameter(s). This can be very challenging and problem dependent. While for the kNDVI the prescription of setting the σ parameter as the average between NIR and red reflectances worked very well, this can be troublesome in other 'kernelized' indices because of the nature of relations between the involved channels.

Table S1: Examples of vegetation indices and their kernel versions.

Indices	**Example**	**VI**	**Kernelized VI**
Ratio	GI (*39*)	$\frac{R_1}{R_2}$	$\frac{k(R_1,R_1)}{k(R_1,R_2)}$
Percentage	IPVI (*40*)	$\frac{R_1}{R_1+R_2}$	$\frac{k(R_1,R_1)}{k(R_1,R_1)+k(R_1,R_2)}$
2-bands	NDVI (*3*)	$\frac{R_1-R_2}{R_1+R_2}$	$\frac{k(R_1,R_1)-k(R_1,R_2)}{k(R_1,R_1)+k(R_1,R_2)}$
3-bands	EVI (*9*)	$\frac{G(R_1-R_2)}{R_1+C_1R_2-C_2R_3+L}$	$\frac{G(k(R_1,R_1)-k(R_1,R_2))}{k(R_1,R_1)+C_1k(R_1,R_2)-C_2k(R_1,R_3)+k(R_1,L)}$
3-bands	VARI (*41*)	$\frac{R_1-R_2}{R_1+R_2-R_3}$	$\frac{k(R_1,R_1)-k(R_1,R_2)}{k(R_1,R_1)+k(R_1,R_2)-k(R_1,R_3)}$
Area	NAOC (*42*)	$1-\frac{\sum_{\lambda=\lambda_1}^{\lambda_2}R_\lambda}{R_2(\lambda_2-\lambda_1)}$	$1-\frac{\sum_{\lambda=\lambda_1}^{\lambda_2}k(R_2,R_\lambda)}{k(R_2,R_2)(\lambda_2-\lambda_1)}$

S2 Mathematical properties of kNDVI

We give some mathematical properties of the kernel NDVI that ensure its generality: the kNDVI generalizes NDVI and NIRv, it captures all (infinite) higher-order moments of the NIR and red band relations when the RBF kernel function is used, the kNDVI adapts to sparsely-vs-densely vegetated areas by means of the kernel parameter, and the index propagates less uncertainty in the spectral bands.

Property S2.1 A kernel vegetation index generalizes its original vegetation index counterpart. *The kernel version of an index reduces to the standard counterpart when linear kernels are used. As an example, using the linear kernels $k(n, r) = n\, r$ and $k(n, n) = n\, n$ into Eq. (1), it is easy to show that the kNDVI reduces to the standard NDVI.*

Property S2.2 The NIR$_v$ in (*20*) is a particular case of kNDVI. *The NIR$_v$ index proposed in (20) departs from the standard NDVI and assumes that pixel reflectance x is composed of a portion δ of vegetation and $1 - \delta$ of soil, i.e. $x = \delta x^v + (1 - \delta)x^s$ for every wavelength λ. Then, by assuming that the soil component remains roughly constant across the spectrum, $n^s \approx r^s$, and that for the vegetation component the NIR reflectance is typically much higher than the red reflectance, $n^v \gg r^v$, one can show that NIR$_v$ $= \delta n^v \approx$ NDVI $\times\, n$. Now, it is easy to show that there exist a σ parameter in the proposed kNDVI that yields the same result as NIR$_v$. Essentially, using an RBF kernel in the kNDVI and isolating σ from the equation*

$$kNDVI = \frac{1 - k(n, r)}{1 + k(n, r)} = NDVI \times n,$$

it is easy to show that using

$$\sigma = \sqrt{\frac{n - r}{2\sqrt{atanh(NDVI\; n))}}}$$

returns NIR$_v$, and therefore demostrating how n$_v$ is a particular case of kNDVI.

Property S2.3 Any kernelized vegetation index with a Gaussian kernel exploits all relations between the considered spectral bands. *We show that replacing a dot product with a kernel function, in particular the Gaussian RBF kernel function, allows us to account for all higher-order moments of similarity between the involved spectral bands. Let us assume the kernel $k(a, b) = \langle \phi(a), \phi(b) \rangle = \exp(-\gamma(a - b)^2)$, where for simplicity we define $\gamma = 1/(2\sigma^2) > 0$. Then, the explicit feature map ϕ is infinite dimensional, and can be expressed as*

$$\phi(a) = \exp(-\gamma a^2) \left[1, \sqrt{\frac{2\gamma}{1!}} a, \sqrt{\frac{(2\gamma)^2}{2!}} a^2, \sqrt{\frac{(2\gamma)^3}{3!}} a^3, \dots \right]^\top.$$

Note that the kernel $k(n, r) = \langle \phi(n), \phi(r) \rangle_{\mathcal{H}}$ is thus a dot product between infinite-dimensional expansions of both n and r, and thus the kernel summarizes the all higher order differences between the NIR and red reflectance bands as $k(n, r) = \sum_{t=0}^{\infty} (-1)^t \gamma^t (n - r)^{2t}/t!$

Figure S2 compares the correlation between SIF and different indices (NDVI, NIRv and kNDVI with polynomial and RBF kernels). Using a polynomial kernel for kNDVI with $p = 1$ recovers the solution of NDVI, while as p increases, higher order relations between the red and NIR bands are captured. In the limit, using the RBF kernel exploits all higher order relations and shows the best correlation, improving results over NIRv.

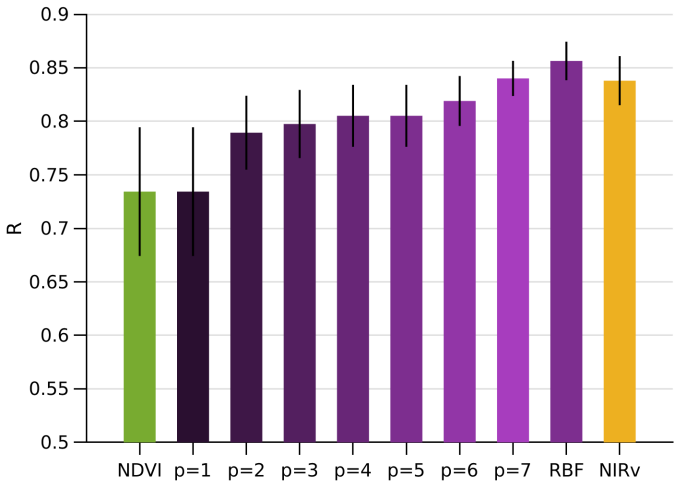

Figure S2: Correlation coefficient R (average and standard deviation) between SIF and the considered indices: NDVI, kNDVI with polynomial and RBF kernels, and NIRv.

Property S2.4 Sensitivity maps of the index. *The derivative of the kNDVI with respect its linear counterpart NDVI, can be easily computed from the complete expression of kNDVI,*

$$\mathrm{kNDVI} = \tanh\left(\left(\frac{n-r}{2\sigma}\right)^2\right) = \tanh\left(\left(\frac{\mathrm{NDVI}}{2\tau}\right)^2\right), \tag{4}$$

where for convenience we used a lengthscale parameter σ that scales linearly with the average of NIR and red reflectances $\sigma = \tau(n + r)$. The derivative can be readily obtained:

$$\frac{d\,\mathrm{kNDVI}}{d\,\mathrm{NDVI}} = \frac{1}{2\tau^2}(1 - \mathrm{kNDVI}^2)\,\mathrm{NDVI}\,.$$

Note that with our recommended value $\tau = 0.5$, the index largely simplifies, $\mathrm{kNDVI} = \tanh(\mathrm{NDVI}^2)$ *and the derivative becomes* $\frac{d\,\mathrm{kNDVI}}{d\,\mathrm{NDVI}} = 2(1 - \mathrm{kNDVI}^2)\,\mathrm{NDVI}\,.$

The value, and thus the sensitivity, of the new index strongly depends of the selected σ (through τ) parameter, see Fig. S3. The higher the σ (or τ) value, the lower the derivative and hence more sensitive to densely vegetated regions. On the contrary, the lower the σ (or τ) value, the more sensitive will be the kernel index to sparsely vegetated regions. The selection of σ has an impact on the

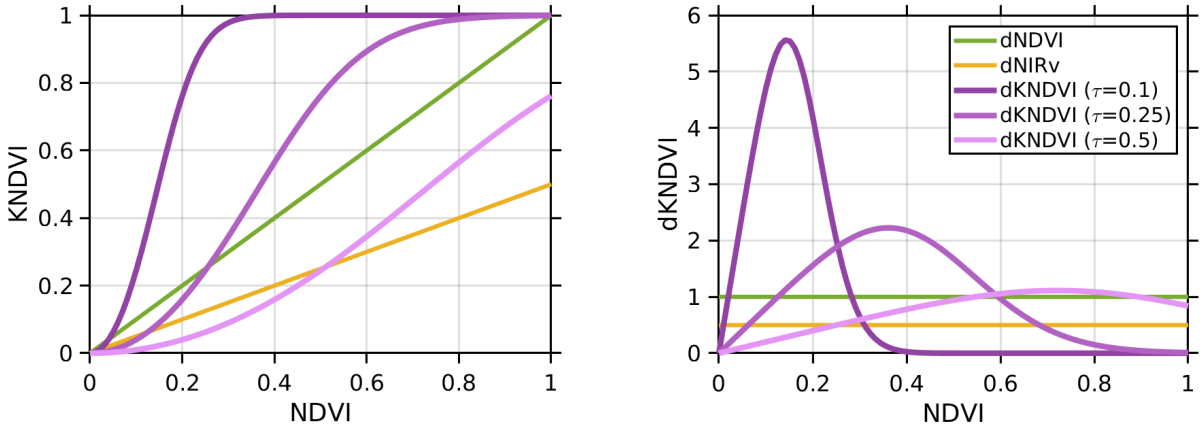

Figure S3: Derivative (sensitivity) of kNDVI and NIRv with respect NDVI (right) and dependence of the indices with NDVI (left) for different values of $\tau \propto \sigma$ (we assumed an arbitrary value of NIR reflectance of 0.5 for the NIRv illustration purposes).

desaturation effect of the index. Lower values of τ would increase the sensitivity to soils and sparsely vegetated pixels. A $\tau = 0.25$ would lead to Gaussian-like sensitivity around NDVI=0.4 but would emphasize too much the lower values and would not reduce the saturation of NDVI at high values. The suggested $\tau = 0.5$, on the contrary, leads to virtually no sensitivity to sparsely vegetated regions (low NDVI, avoiding the bias problem), then varies roughly linearly with NDVI for mixed-pixels (moderate NDVI) and then decreases for highly vegetated regions (high NDVI, reducing the NDVI saturation problem). Note that, unlike NIRv whose sensitivity increases linearly with NIR, the kNDVI with $\sigma = 0.5(n + r)$ copes with the saturation problem with a nonlinear function. In principle, one could optimize the τ value per biome of climatic region to increase the sensitivity or reduce the bias. In our experiments, however, $\tau = 0.5$ showed a good compromise between accuracy and simplicity.

Property S2.5 Error propagation. *Let us compare the indices in terms of uncertainty propagation in the spectral bands. Given the transformation* $\mathrm{kNDVI} = \tanh(((n-r)/(2\sigma))^2)$*, and independent distortions in each channel with standard deviations* σ_n *and* σ_r*, one can calculate the first order linear approximation of the error propagation by using the variance formula:*

$$\sigma^2(\mathrm{kNDVI}) = \left(\frac{d\,\mathrm{kNDVI}}{dn}\right)^2 \sigma_n^2 + \left(\frac{d\,\mathrm{kNDVI}}{dr}\right)^2 \sigma_r^2,$$

where the derivatives of kNDVI with respect the reflectances of the NIR and the red bands are:

$$\frac{d\,\mathrm{kNDVI}}{dn} = \frac{(n-r)}{2\sigma^2} sech^2\left(\left(\frac{n-r}{2\sigma}\right)^2\right) \quad \textit{and} \quad \frac{d\,\mathrm{kNDVI}}{dr} = -\frac{(n-r)}{2\sigma^2} sech^2\left(\left(\frac{n-r}{2\sigma}\right)^2\right).$$

The error propagation for the NDVI involve

$$\frac{d\,\mathrm{NDVI}}{dn} = \frac{2r^2}{(n+r)^2} \quad \textit{and} \quad \frac{d\,\mathrm{NDVI}}{dr} = -\frac{2n^2}{(n+r)^2}$$

and for the NIRv involve

$$\frac{d\,\mathrm{NIRv}}{dn} = \frac{(n^2 + 2nr - r^2)}{(n+r)^2} \quad \textit{and} \quad \frac{d\,\mathrm{NIRv}}{dr} = -\frac{2n^2}{(n+r)^2}.$$

See a comparison between the three indices in Fig. S4. Results suggest that the kNDVI propagates a lower amount of error than the rest of the indices, especially resistant to increased noise variance, which may result in more robust estimates.

(a) $\sigma_n = \sigma_r = 0.01$ (b) $\sigma_n = \sigma_r = 0.05$ (c) $\sigma_n = \sigma_r = 0.10$

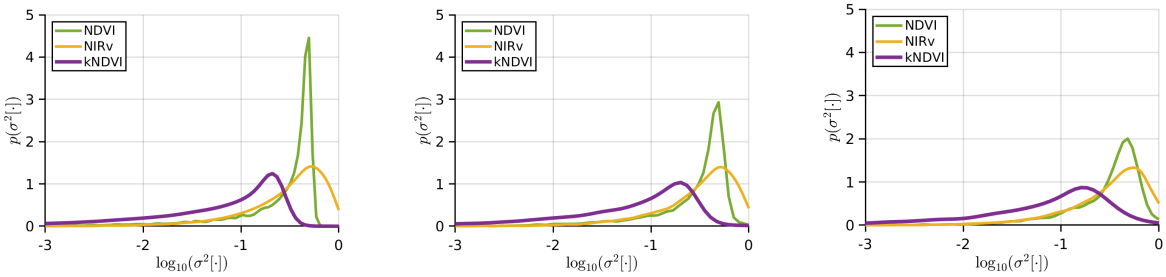

Figure S4: Density p of the propagated errors by all indices (σ^2[NDVI], σ^2[NIRv] and σ^2[kNDVI]) over a uniform grid of 10^4 combinations of NIR and red reflectance values, and fixing $\sigma_n = \sigma_r$ to 0.01 (a), 0.05 (b) and 0.1 (c) standard deviation of additive white Gaussian noise (distortion/error level) in each channel.

S3 IGBP groups

Table S2: IGBP classification.

Class	IGBP	Acronym
0	Water	WAT
1	Evergreen Needleleaf Forest	ENF
2	Evergreen Broadleaf Forest	EBF
3	Deciduous Needleleaf Forest	DNF
4	Deciduous Broadleaf Forest	DBF
5	Mixed Forest	MF
6	Close Shrublands	CSH
7	Open Shrublands	OSH
8	Woody savannas	WSA
9	Savannas	SAV
10	Grasslands	GRA
11	Permanent wetlands	WET
12	Croplands	CRO
13	Urban and built-up	URB
14	Cropland/Natural vegetation mosaic	CVM
15	Snow and ice	SNO
16	Barren or sparsely vegetated	BSV

Table S3: The considered IGBP classes and their grouping in our study.

Class	Name	Acronym	IGBP classes cf. S2 merged
C1	Needleleaf Forest	NF	1+3
C2	Evergreen Broadleaf Forest	EBF	2
C3	Deciduous Broadleaf Forest	DBF	4
C4	Mixed forest	MF	5
C5	Shrublands	SH	6+7
C6	Savannas	SAV	8+9
C7	Herbaceous	GRA	10
C8	Cultivated	CRO	12

S4 Correlation with remotely-sensed Leaf Area Index (LAI)

LAI is a key biophysical parameter for both Earth vegetation modelling and monitoring. Many studies have reported nonlinear empirical relations between NDVI and LAI. However, it is acknowledged that this relation varies temporally according to the phenological development of plants and trees, as well as with the changing environmental conditions (*43*). The correlation of kNDVI with LAI, also compared to both NDVI and NIRv, is presented here.

S4.1 LAI data and surface reflectances

The MCD43A4 and MCD15A3H MODIS v006 products were used as reflectance data and LAI estimates, respectively. Both satellite products are provided at 500 m spatial resolution and generated combining data from Terra and Aqua spacecrafts. They are disseminated from the Land Processes Distributed Active Archive Center (LP DAAC) also available at Google Earth Engine (GEE). MCD43A4 offers a daily global Bidirectional Reflectance Distribution Function (BRDF) product from a Nadir view in seven MODIS land bands (red, near infrared, blue, green, short wave infrared-1, short wave infrared-2, and middle wave infrared). The MCD43A2 MODIS product, which contains the quality information for the corresponding MCD43A4 product, was also used for avoiding low-quality BRDF estimates. The MCD15A3H collection 6 product provides LAI estimates every 4 days, and uses for the retrieval a look-up-table (LUT) approach simulated from a 3-D radiative transfer model. The product also provides with a quality flag information of the LAI estimates.

S4.2 Processing

We used GEE for processing the MODIS products' time series over 445 global biome-representative sites from July 4, 2002 to March 14, 2017. The selected sites belong to the BEnchmark Land Multisite ANalysis and Intercomparison of Products dataset (BELMANIP) (*44*). It was built using 420 sites from existing experimental networks (FLUXNET, AERONET, VALERI, BigFoot, etc) completed with selected sites from the GLC2000 land cover map. The updated one, BELMANIP2.1 dataset complements BELMANIP by adding 25 sites corresponding to bare soil areas (deserts) and tropical forests (Figure S5). Site selection was performed by keeping the same proportion of biome types within the selected sites as within the 10^o-width latitudinal bands. Attention was paid so that the sites were homogeneous over a $10\times$ 10 km^2 area, almost flat, and with a minimum proportion of urban area and permanent water bodies.

Since the used MODIS products differ in temporal frequency of production, only coincident dates among them were selected. The MCD43A4 was used to compute the indices after filtering non-valid pixels. This was carried out excluding clouds, cloud shadows, snow, as well as poor-quality BRDF parameter retrievals according to the pixel-based quality flag provided by the MCD43A2 MODIS product, which is also available in GEE. In addition, only LAI estimates provided by the MCD15A3H main algorithm were used, and intentionally filtered out estimates from the back-up algorithm as they

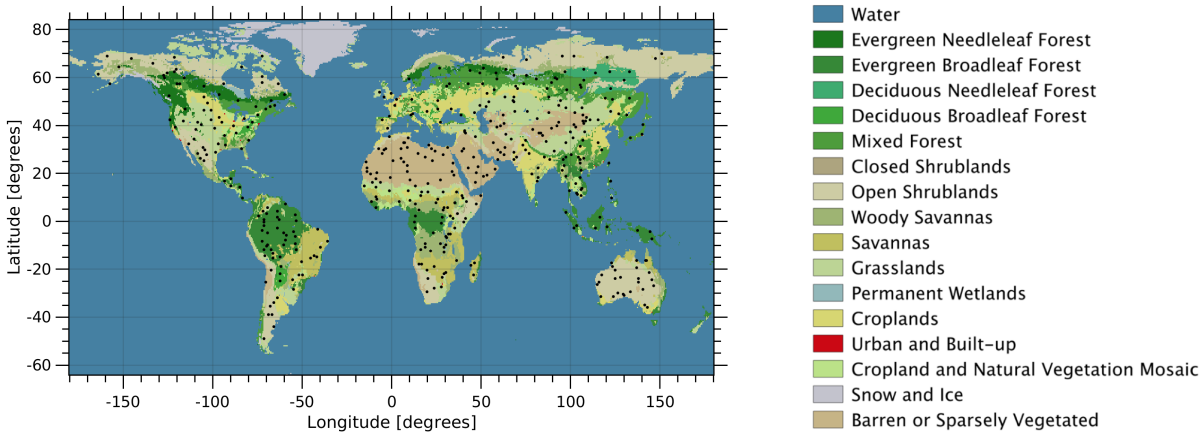

Figure S5: Location of the BELMANIP2.1 sites and associated biomes.

internally use NDVI and related biophysical parameters. Hence, we did not use MODIS-derived LAI estimates that can be affected by NDVI to avoid biased results and conclusions. This yielded 60,078 observations. LAI correlations with kNDVI, NIRv, and NDVI, were computed using these observations in the temporal domain. Lastly, the correlations are also reported per global biomes.

S4.3 Results

We evaluated our proposed kNDVI as a proxy for LAI over a large dataset of MODIS LAI estimates. Results indicate that kNDVI (R=0.81) correlates better with the MODIS LAI product than NDVI (R =0.74) and NIRv (R=0.76), see details in Table S4. These results are observed over all biomes and conditions (Fig. S6).

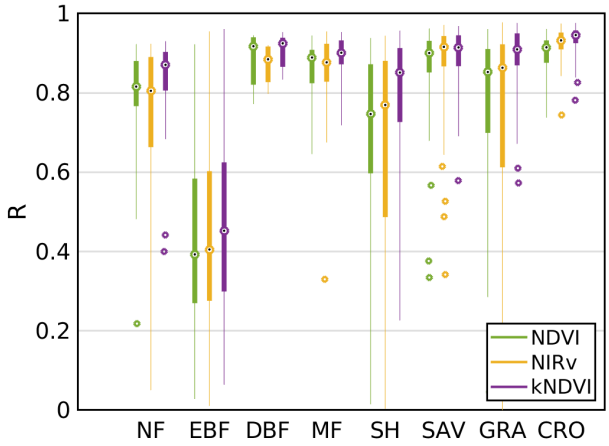

Figure S6: Boxplots of the averaged correlations between LAI and NDVI, NIRv and, kNDVI per biome type.

Table S4: Correlation coefficient between the three vegetation indices (NDVI, NIRv, kNDVI) and LAI per biome. Darker green indicates higher correlation values.

		LAI		
	Biome	**NDVI**	**NIRv**	**kNDVI**
C1	**NF**	0.75	0.79	**0.82**
C2	**EBF**	0.41	0.43	**0.45**
C3	**DBF**	0.87	0.88	**0.91**
C4	**MF**	0.85	0.86	**0.89**
C5	**SH**	0.63	0.67	**0.79**
C6	**SAV**	0.86	0.87	**0.89**
C7	**GRA**	0.74	0.79	**0.89**
C8	**CRO**	0.90	0.93	**0.94**
	ALL	0.74	0.76	**0.81**

Assessment per biome type reveals kNDVI as the most correlated index wih LAI (see Fig. S6). In general the correlations are high, except over EBF the correlation is clearly lower. This can be due to the fact that the MODIS LAI retrieval rate of the main algorithm is very low in the case of EBF caused by reflectance saturation (*45*). In addition, the distribution of correlations reveals that kNDVI outperforms both NDVI and NIRv (Fig. S7).

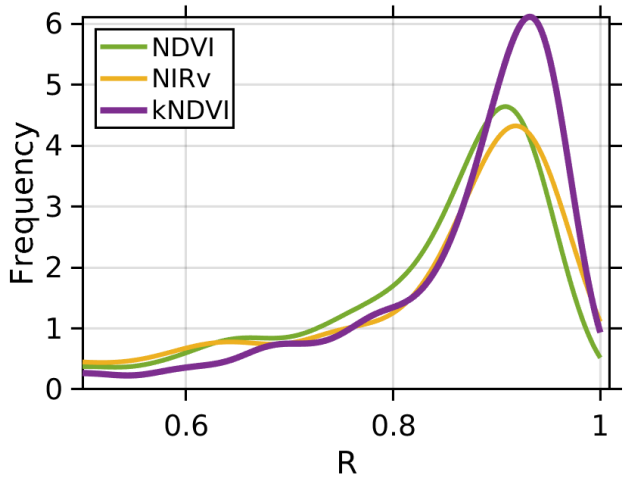

Figure S7: Estimated density of the correlation coefficient between the indices and LAI.

We show the temporal evolution of the considered indices and LAI over both cultivated and herbaceous areas, see Fig. S8. The time series reveal that kNDVI follows similarly the LAI temporal behaviour whereas NDVI performance is worse mainly in sparse vegetation periods. The index actually

adapts better to phenological cycles, and is more sensitive to low vegetation too (see Fig. S8). The kNDVI values are close to zero when no (or sparse) vegetation is present, whereas NDVI systematically retrieves values around 0.2. This highlights the normalization power of kNDVI in very early phenological stages that present high brightness variability in the underlying soil background.

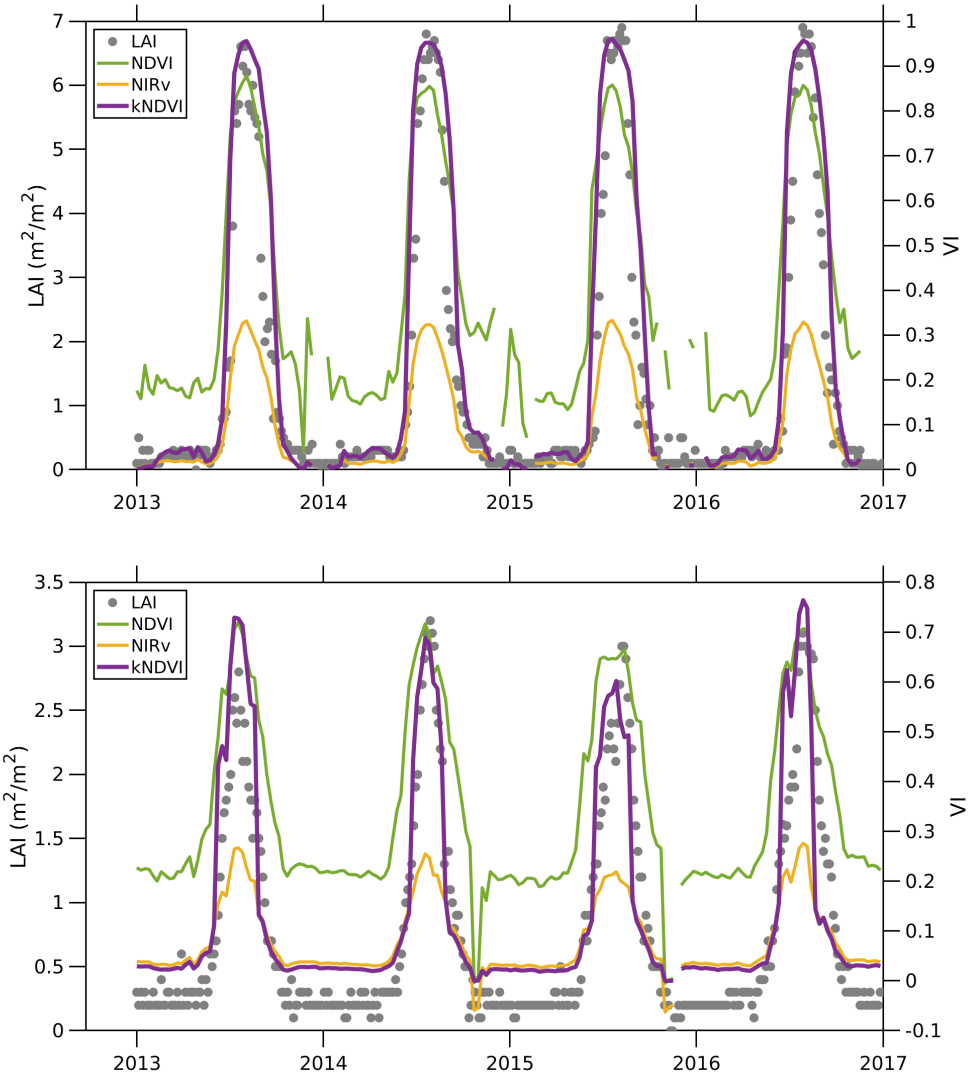

Figure S8: Time series over a cultivated area (top) and an herbaceous area (bottom) in the BELMANIP2.1 collection during the period 2013-2016.

S5 Additional analysis of GPP results

S5.1 Quantification of tower-level correlations per biome type

The per biome type assessment reveals that kNDVI generally outperforms the rest of VIs to predict GPP estimates over 4 of 7 considered biomes types (see Fig. S9). Correlations are moderate to high in all biomes, except for the EBF biome type where none of the considered VI performs adequately. This can be attributed to reflectance saturation issues (*45*)

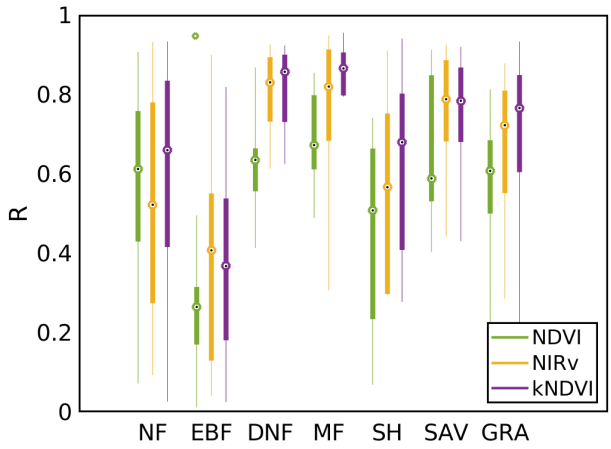

Figure S9: Boxplots of correlations between GPP and NDVI, NIRv and, kNDVI per biome type.

S5.2 On the linearization effect of normalizing GPP with radiation

Here we compare the effect of normalizing the GPP by PAR on the indices performance. Table S5 shows the results of association between the different indices (NDVI, NIRv and kNDVI) on both situations (GPP and GPP/PAR). In the comparison we used different measures of association (that is, statistical dependence) both linear and nonlinear; Pearson's correlation coefficient R; Spearman's correlation coefficient, RS (*26*); Mutual information, MI (*27*); and Distance Correlation, DC (*28*). Such analysis is imperative to have a clear view of the impact of the normalization on the indices.

S5.2.1 On the linearization via normalization versus the implicit linearization via kernels.

Results suggest that normalizing GPP by PAR has an obvious linearization effect since differences between indices are smaller independently of the dependence measure used (note that while tempting, one should not compare the scores obtained in the normalized versus the unnormalized case as a nonlinear transformation is applied and they cast different problems now). It is also observed that such normalization affects NIRv the most, which yields virtually no numerical difference with NDVI. A noticeable gain is still obtained with the proposed kNDVI. After all, kernel methods in general, and

Table S5: Average results obtained with different measures of dependence between the indices and GPP or GPP/PAR.

	GPP			GPP/PAR		
	NDVI	**NIRv**	**kNDVI**	**NDVI**	**NIRv**	**kNDVI**
R	0.59	0.68	**0.68**	0.58	0.58	**0.60**
RS	0.62	**0.66**	0.63	0.58	0.56	**0.58**
MI	0.31	0.46	**0.47**	0.33	0.34	**0.36**
DC	0.64	0.71	**0.71**	0.65	0.65	**0.66**

the kNDVI in particular, implement the original operation –the NDVI– in a feature space where NIR and red have been mapped to. The kNDVI is a linear operation in that space, which is nonlinear in the original (bands) input space. The simplicity and elegance of the framework allows us to accomplish the ever-sought linearization transformation implicitly. This means that no *ad hoc* parametric transformations are needed, just the kernel trick (*25, 46*). But, this also implies that virtually no gain over other indices will be obtained when the relation between the bands and the parameter of interest is linear, such as for instance after PAR normalization or when working (averaging) over larger spatial or temporal scales (see S6.3). Our results showed that the kNDVI improved results in all cases but, as expected, the gain was moderate when the domain was previously linearized.

S5.2.2 On the linear versus nonlinear regime

GPP is routinely estimated from satellite data with the light use efficiency (LUE) model (*47,48,49,50*). It is a simple model which consists of the product of the photosynthetically active radiation (PAR), the fraction of PAR absorbed by the vegetation (fAPAR), and an energy conversion efficiency factor or LUE. Within the LUE modelling logic, the fAPAR (often calculated as a linear function of the NDVI) is in charge of capturing the dynamics in photosynthetic biomass (green leaves, green stems, and shoots), while the LUE and PAR variables provide the relationship between GPP and light. However, the LUE model assumes a linear relationship between the GPP and the absorbed PAR, which is valid in a broad range of biomes and environmental conditions but breaks at high temporal resolutions (daily variation) due to nonlinear asymptotic light saturation effects, which is not the case of the present study. This seems to be the reason why the weekly GPP/PAR appears not to be greatly benefited by using higher-order (nonlinear) approaches like the kNDVI.

S6 Additional analysis of SIF results

S6.1 Spatial correlations

An alternative study with SIF was done computing the spatial correlation and averaging results through time. The overall average correlation over the 506 images (16-daily, 0.5^o), see Table S6, shows outstanding results of kNDVI ($R = 0.84$) over NDVI ($R = 0.69$), and improves performance over NIRv ($R = 0.81$). The kNDVI excels in characterizing all vegetation types (gains in R of +21.7% over NDVI and +3.7 over NIRv). Interestingly, in needle-leaf forests, kNDVI largely improves NDVI (gain of +18.5%) but performs slightly worse than NIRv (-6.7%). Accuracy of the kNDVI ($R = 0.82$) is also higher than NDVI ($R = 0.64$) or NIRv ($R = 0.80$) at different latitudes, yet far more noticeable in higher latitudes ($\geq 30^o$). This matches results when disaggregated by climatic zones (Köppen regions): the index achieves averaged improvements in correlation above +35% with regard to the NDVI and around +3% over NIRv in cold regions.

Table S6: Spatial correlation coefficients between the vegetation indices and SIF per biome. Greener colors indicate higher correlations.

		Spatial SIF		
	Biome	**NDVI**	**NIRv**	**kNDVI**
C1	**NF**	0.63	**0.80**	0.74
C2	**EBF**	0.65	0.79	**0.81**
C3	**DBF**	0.49	**0.53**	0.51
C4	**MF**	0.59	0.75	**0.77**
C5	**SH**	0.65	0.82	**0.84**
C6	**SAV**	0.77	0.83	**0.84**
C7	**GRA**	0.72	0.82	**0.84**
C8	**CRO**	0.71	0.83	**0.85**
	ALL	0.69	0.81	**0.84**

S6.2 Monthly and seasonal correlations

Figure S10 shows the obtained correlations between the indices and SIF for the whole period 2007-2018 grouped by month and season. kNDVI and NIRv perform similarly in all cases and much better than NDVI. A noticeable gain is observed during the SON months and Fall season.

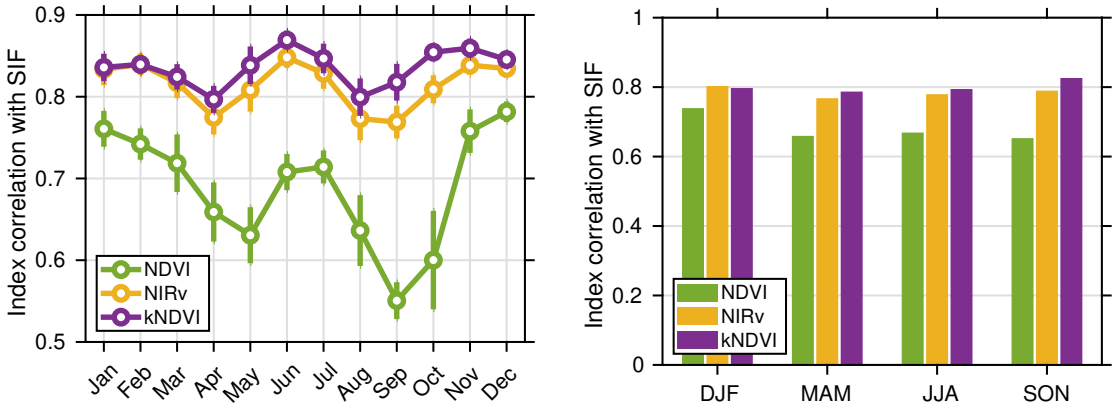

Figure S10: Monthly correlations between the index and SIF for all considered biomes and all 10 years of data (left) and analysis per season (right).

S6.3 Impact of spatial and temporal scales

We analyze here the correlation between SIF and the indices at different temporal (biweekly, monthly and bimonthly) and spatial (0.5, 1, 2) scales, see Fig. S11. Results confirm that kNDVI is more competitive at finer temporal resolutions with a noticeable advantage over NDVI (+15%) and NIRv (+4%), but the gain over NIRv disappears at bimonthly scales. A broader spatial aggregation tends to improve results of all indices and kNDVI outperforms the others independently of the spatial scale.

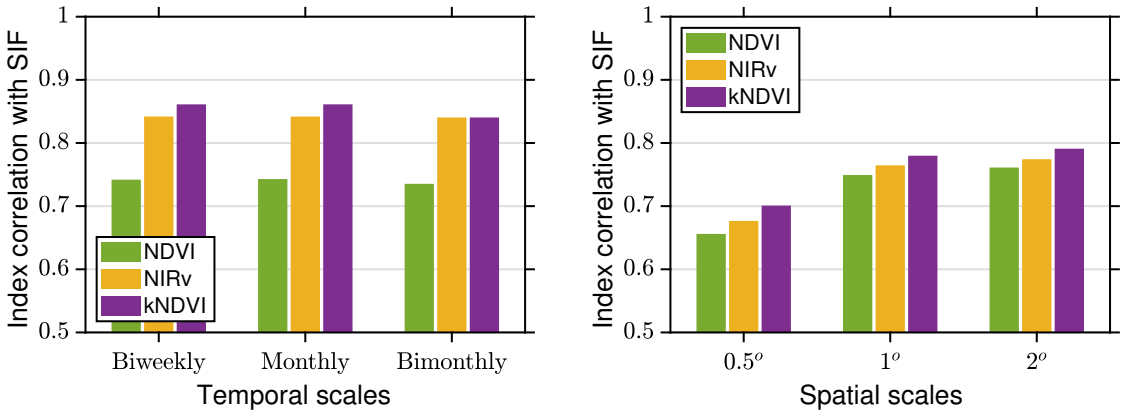

Figure S11: Average global correlation between the indices and SIF at different temporal (biweekly, monthly and bimonthly) and spatial (0.5, 1, 2) scales.

S6.4 On the linearization effect of normalizing SIF with radiation

Here we study the impact of considering SIF normalized by radiation instead of the raw SIF (to create an expression of "SIF efficiency"). In our study we approximated PAR with the cos(SZA) and studied the effect of such normalization, PAR/cos(SZA), on the results. The idea behind this is to 'discount' the associations due to seasonality. In the unnormalized case, the nonlinear similarity measures (Spearman, mutual information, and distance correlation) agree with Pearson's correlation, and are favourable to kNDVI, see Table S7. When SIF is normalized, all measures still indicate that the proposed kNDVI aligns better, yet results are deemed similar to NIRv. Note that kernel methods in general, and kNDVI in particular, solve a linear problem in a nonlinearly transformed space. Since the main effect of dividing SIF by the cos(SZA) is to linearize the problem, getting rid of the strong nonlinear seasonal cycle that dominates the distribution, a significant improvement over NIRv is not expected. Yet, still for all measures the index tends to generalize (improve) both indices. These results are also observed per biome (see Table S8), climate zone (see Table S9) and latitude (see Table S10).

Table S7: Average results over time obtained with different measures of dependence between the indices and SIF or SIF/cos(SZA) as a proxy to PAR normalization. Greener colors indicate higher values of linear and nonlinear association.

	SIF			SIF/cos(SZA)		
	NDVI	**NIRv**	**kNDVI**	**NDVI**	**NIRv**	**kNDVI**
R	0.54	0.63	**0.65**	0.55	0.58	**0.59**
RS	0.53	0.62	**0.65**	0.55	0.58	**0.59**
MI	0.33	0.43	**0.45**	0.34	0.37	**0.38**
DC	0.59	0.65	**0.67**	0.60	0.62	**0.63**

Table S8: Averaged temporal correlation between the indices and SIF/cos(SZA) per biome. Greener colors indicate better linear and nonlinear association values.

		R			RS			MI			DC		
	Biome	**NDVI**	**NIRv**	**kNDVI**	**NDVI**	**NIRv**	**kNDVI**	**NDVI**	**NIRv**	**kNDVI**	**NDVI**	**NIRv**	**kNDVI**
C1	**NF**	0.65	0.69	**0.70**	0.67	0.69	**0.70**	0.39	0.44	**0.44**	0.69	0.71	**0.71**
C2	**EBF**	0.65	0.69	**0.69**	0.67	**0.70**	**0.70**	0.41	0.46	**0.46**	0.69	**0.72**	**0.72**
C3	**DBF**	**0.46**	0.45	0.40	**0.47**	0.45	0.39	**0.21**	**0.21**	0.19	**0.49**	0.47	0.44
C4	**MF**	0.60	0.64	**0.65**	0.61	**0.64**	**0.64**	0.38	0.42	**0.43**	0.64	0.66	**0.66**
C5	**SH**	0.63	0.66	**0.67**	0.63	**0.66**	**0.66**	0.39	0.43	**0.43**	0.67	0.69	**0.69**
C6	**SAV**	**0.57**	0.56	0.55	**0.57**	0.56	0.54	**0.34**	**0.34**	**0.34**	**0.60**	0.59	0.59
C7	**GRA**	0.50	0.55	**0.58**	0.50	0.55	**0.58**	0.29	0.33	**0.34**	0.55	0.58	**0.60**
C8	**CRO**	0.54	0.59	**0.61**	0.55	0.59	**0.60**	0.30	0.34	**0.35**	0.58	0.61	**0.62**
	ALL	0.55	0.58	**0.59**	0.55	0.58	**0.59**	0.34	**0.37**	**0.37**	0.60	**0.62**	**0.62**

Table S9: Correlation between the indices and SIF (left) or SIF/cos(SZA) (right) per climate zone. Greener colors indicate higher correlations.

	SIF			SIF/cos(SZA)		
Climatic zone	**NDVI**	**NIRv**	**kNDVI**	**NDVI**	**NIRv**	**kNDVI**
A- Tropical	0.59	0.68	**0.69**	0.61	**0.65**	**0.65**
B- Arid	0.47	0.55	**0.61**	0.49	0.51	**0.56**
C- Temperate	0.61	0.72	**0.74**	0.61	0.63	**0.65**
D- Cold	0.51	0.59	**0.66**	0.53	0.55	**0.62**
E- Polar	0.66	0.74	**0.77**	0.70	**0.72**	**0.72**

Table S10: Temporal correlation between the indices SIF (left) or SIF/cos(SZA) (right) per latitude. Greener colors indicate higher correlations.

			SIF		SIF/cos(SZA)		
Latitude range		**NDVI**	**NIRv**	**kNDVI**	**NDVI**	**NIRv**	**kNDVI**
-60	-30	0.43	0.54	**0.59**	**0.53**	**0.53**	0.49
-30	0	0.50	0.57	**0.58**	**0.52**	**0.52**	**0.52**
0	30	0.65	0.73	**0.75**	0.66	0.69	**0.70**
30	60	0.53	0.61	**0.67**	0.53	0.58	**0.62**
60	90	0.64	0.72	**0.73**	0.65	0.68	**0.69**

S7 Dependence between the index and in-situ Chlorophyll content, LAI and FVC

We quantitatively assess the performance of kNDVI in real *in situ* measurements of chlorophyll content (Chl-a), leaf-area index (LAI) and fractional vegetation cover (FVC). For this purpose, we will use the SPARC dataset (*51, 52*). The SPectra bARrax Campaign (SPARC) field dataset encompasses different crop types, growing phases, canopy geometries and soil conditions. The SPARC-2003 campaign took place from 12 to 14 July in Barrax, La Mancha, Spain (coordinates 30°3'N, 28°6'W, 700 m altitude). Bio-geophysical parameters have been measured within a total of 108 Elementary Sampling Units (ESUs) for different crop types (garlic, alfalfa, onion, sunflower, corn, potato, sugar beet, vineyard and wheat). An ESU refers to a plot, which is sized compatible with pixel dimensions of about 20 m $\times$ 20 m. In the analysis no differentiation between crops was made.

Table S11: Linear and nonlinear dependence measures between the vegetation indices and the biophysical parameter.

		NDVI	NIRv	kNDVI
R	**LAI**	0.71	0.72	**0.78**
	fAPAR	0.75	0.83	**0.86**
	FVC	0.85	0.86	**0.88**
RS	**LAI**	0.45	**0.52**	0.50
	fAPAR	0.70	0.83	**0.85**
	FVC	0.63	0.79	**0.81**
MI	**LAI**	0.33	0.37	**0.47**
	fAPAR	0.41	0.59	**0.67**
	FVC	0.63	0.66	**0.73**
DC	**LAI**	0.69	0.72	**0.74**
	fAPAR	0.79	0.84	**0.85**
	FVC	0.82	0.83	**0.86**
MSE	**LAI**	9.44	9.95	**9.00**
	fAPAR	1.00	0.83	**0.77**
	FVC	0.17	0.16	**0.15**

The data used in this study were obtained in two terrestrial campaigns in Barrax, Spain. The test area has a rectangular form and an extent of 5 km $\times$ 10 km, and is characterized by a flat morphology and large, uniform land-use units. The region consists of approximately 65% dry land and 35% irrigated land. Several instruments were used to measure the variables: a calibrated CCM-200 Chlorophyll Content Meter for Chl-a, the LiCor LAI-2000 for LAI, and hemispherical photographs taken with a digital camera with a fish-eye lens for FVC. Simultaneously we used satellite images from the CHRIS sensor. CHRIS measures over the visible/ near-infrared spectra from 400 to 1050 nm. For this study, we used CHRIS data in Mode 1 (62 bands, full spectral information) for the four campaign days, where *in situ* measurements of surface properties were measured in conjunction with the satellite overpass. The images were geometrically and atmospherically corrected. Three sets of 135 measurements were collected in total. Results are shown in Table S11, where again kNDVI is a better proxy of the different *in situ* measurements of biophysical parameters, independently of the adopted measure: higher values of Pearson's correlation R; Spearman's correlation, RS; Mutual information, MI; and Distance Correlation, DC; and lower values of MSE of a linear fit indicate better performance.

S8 Crop yield estimation

Accurate and timely crop yield estimation is currently one of the major challenges in agricultural research and of paramount interest to governments, public administrations, and farm managers (*53*, *54*, *55*). Earth observation (EO) data has opened new ways for efficient agricultural mapping, crop monitoring and assessment, as it allows deriving spatially explicit and temporally resolved maps of production and yield (*56*, *57*). Most studies on the use EO data for crop estimation are centered on visible and infrared sensors. Actually, optical vegetation indices are easy to compute and useful to monitor the quantity, quality and behavior of the vegetation representing the intra-annual vegetation dynamics (*58*, *59*, *60*). Among the most widely used VIs, the NDVI has been extensively and successfully used in agricultural mapping and monitoring, as well as in many crop yield studies (*61*, *62*, *63*, *64*, *65*).

We used five years of Multi-angle Imaging SpectroRadiometer (MISR) data over the state of Kansas (US) in the "corn belt" and derived weekly averaged time series of NDVI, NIRV and kNDVI at county scale. A total of 79 time series with co-located yield were used for 13 counties. The goal is to estimate the crop yield of both corn and wheat from the time series. The target yield comes from the U.S. Department of Agriculture (USDA) records. To evaluate the indices, we developed an extremely simple crop yield estimation model: the index time series were used as a feature vector to fit a linear regression model. We then computed the correlation coefficient between the estimated and the surveyed USDA crop yield. We also measured the maximum correlation obtained between each index and the yield, as a measure of estimation power. Results are given in Table S12. In both approaches, the kNDVI improves results over the other indices.

Table S12: Correlation coefficient between the estimated and the surveyed crop yield in two settings: (left) using the year time series in a multivariate linear regression (MLR); and (right) maximum correlation between the weekly observation and the yield.

	MLR	**R_{max} (week)**
Corn		
NDVI	0.5591	0.1960 (23)
NIRv	0.5967	0.2446 (29)
kNDVI	0.6157	0.2775 (29)
Wheat		
NDVI	0.7001	0.1591 (39)
NIRv	0.7195	0.3134 (39)
kNDVI	0.7530	0.3598 (39)

The RMSE (bushels/acre) of each model can be translated into actual production (in bushels) by normalizing over the acres planted. Information obtained from USDA.gov. Results are shown in Table S13, and reveal that the lower error obtained by using kNDVI in the linear prediction model generally translates into lower production estimates (around 330'000 bushels/year of corn and 400'000 bushels/year of wheat) compared to the standard NDVI.

Table S13: Translation of RMSE (bushels/acre) into bushels for the particular example of using a linear regression for yield estimation over Kansas.

Corn	NDVI	NIRv	kNDVI
RMSE (bushels/acre)	15.9352	16.123	15.8321
RMSE (bushels)	52108104	52722210	51770967
Diff relative to NDVI (bushels)	-	614106	-337137
Wheat	NDVI	NIRv	kNDVI
RMSE (bushels/acre)	8.3266	8.7451	8.2861
RMSE (bushels)	83682330	87888255	83275305
Diff relative to NDVI (bushels)	-	4205925	-407025

S9 Change detection

We show results of applying vegetation indices in the detection of changes in multispectral Sentinel-2b images. Two scenes are considered: natural floods caused by cyclone Debbie in Australia 2017, and consequences of wildfires in a mountainous area of California (USA), see Fig. S12. Following the standard change vector analysis (CVA) procedure, we used the absolute difference of the vegetation indices between the pre- and post-event dates as the anomaly detector.

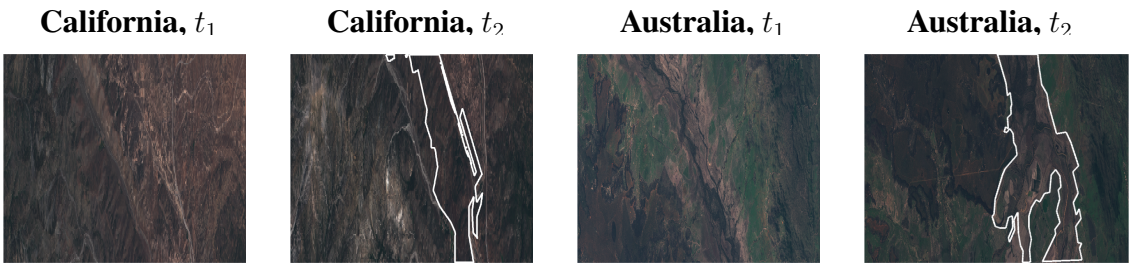

Figure S12: RGB composite S2-b pre- and post-event images of California wildfires (left) and Australia floods (right). The changed area boundary is highlighted in white, and used for computing the ROC and AUC. **Credits:** Images are freely available from ESA Copernicus Hub.

Figure S13 shows the Receiver Operating Curves (ROCs) of the indices, the area under the curves (AUC), and the change detection maps. It can be noted that the kNDVI achieves an improved detection performance over NDVI and NIRv, especially noticeable in the false positive rate regimes. This can be confirmed in the detection images, where kNDVI provides sharper detection maps.

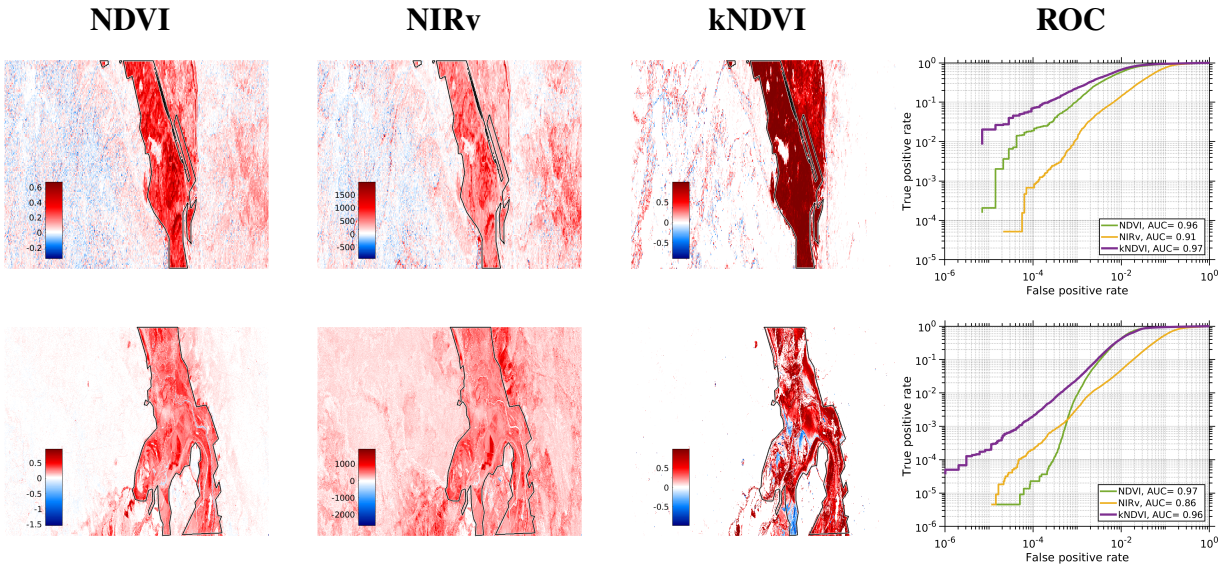

Figure S13: Difference maps by each index for California wildfires (top row) and Australia floods (bottom row) scenes. The difference is taken as the change indicator to compute the ROC and AUC (right plots).

S10 Source code implementation

The kernel-based vegetation indices can be easily programmed and applied. Here we give implementations in standard programming languages. We provide updated code snippets in MATLAB, R, Python, Julia, and IDL, as well as prescriptions and recommendations on the use of the index and the (important) selection of σ, in this GitHub site. Simple demos in Google Earth Engine (GEE) are available in the following GEE link.

In all cases, and for illustration purposes, we used the standard RBF kernel function in the kNDVI, and fixed σ to an arbitrary value of 0.15. In our experiments, we used a common heuristic in machine learning that fixes σ to the mean distance between the involved objects in the kernel similarity measure, in our case the NIR and red bands. Optimization of σ, e.g. per biome or climatic region, is also possible. However, this simple heuristic performed very well in our experiments.

S10.1 MATLAB

Given the NIR and RED values for a particular pixel in scalar MATLAB variables `xn` and `xr`, the kNDVI is computed as:

```
sigma = 0.15;
knr = exp(-(xn-xr)^2/(2*sigma^2));
kndvi = (1-knr)/(1+knr);
```

Listing 1: MATLAB code snippet for the kNDVI index

which can be easily computed for a whole image using right array divisions on bands.

S10.2 R

```
sigma <- 0.15
knr <- exp(-(xn-xr)^2/(2*sigma^2))
kndvi <- (1-knr) / (1+knr)
```

Listing 2: R code snippet for the kNDVI index

S10.3 Python

```
import numpy as np
sigma = 0.15
knr = np.exp(-(xn-xr)**2/(2*sigma**2))
kndvi = (1-knr) / (1+knr)
```

Listing 3: Python code snippet for the kNDVI index

S10.4 Julia

```
sigma = 0.15
knr = exp(-(xn-xr)^2 / (2*sigma^2))
```

```
kndvi = (1-knr) / (1+knr)
```

Listing 4: Julia code snippet for the kNDVI index

S10.5 IDL

Similarly to the MATLAB code, given an image loaded in IDL environment and the NIR and RED bands assigned to `nir` and `red` variables, the kNDVI is computed as:

```
sigma = 0.15
k = exp(-( nir*1.0-red )^2/(2*sigma^2))
kNDVI = (1-k)/(1+k)
```

Listing 5: IDL code snippet for the kNDVI index

S10.6 Google Earth Engine (GEE)

Given the NIR and red bands identified by the variables `nir` and `red`, the kNDVI is computed using a map function defined as:

```
// Javacript for GEE
// The example here assumes the values of these bands are *reflectances*.
// For instace, for MODIS you must divide the raw values by 10000.
// See the image collection documentation for specific instructions.
// We present two implementations which are equivalent:
//      1. Using the definition of the RBF kernel k(nir,red)=exp(-(nir-red)^2...
   /(2*sigma^2)) in the kNDVI=(1-k(nir,red))/(1+k(nir,red))
//      2. which is equivalent to kNDVI = tanh((nir-red)^2/(2*sigma)^2)
// Both obtain the same result, use the one you prefer!

var addKNDVI_RBF = function(image) {
  // Compute (nir-red)^2
  var D2 = nir.subtract(red).pow(2);
  // Fix or estimate a reasonable sigma value, e.g. sigma = 0.15
  var sigma = ee.Number(0.15);
  // Compute kernel (k) and kNDVI
  var k = D2.divide(sigma.pow(2)).multiply(-1).exp();
  var kndvi = ee.Image.constant(1).subtract(k)
      .divide(ee.Image.constant(1).add(k));
  return image.addBands(kndvi.select([0], ['kndvi']));
}

var addKNDVI_tanh = function(image) {
  // Compute (nir-red)^2
  var D2 = nir.subtract(red).pow(2);
  var sigma = ee.Number(0.15);
  var kndvi = D2.divide(sigma.multiply(2.0).pow(2)).tanh();
  return image.addBands(kndvi.select([0], ['kndvi']));
}
```

Listing 6: GEE/JavaScript code snippet for the kNDVI index